The Astrophysical Journal, 695:596–618, 2009 April 10 doi:10.1088/0004-637X/695/1/596

MULTIWAVELENGTH OBSERVATIONS OF MARKARIAN 421 IN 2005–2006

D. Horan[1], V. A. Acciari[2,3], S. M. Bradbury[4], J. H. Buckley[5], V. Bugaev[5], K. L. Byrum[1], A. Cannon[6], O. Celik[7], A. Cesarini[8], Y. C. K. Chow[7], L. Ciupik[9], P. Cogan[10], A. D. Falcone[11], S. J. Fegan[7], J. P. Finley[12], P. Fortin[13], L. F. Fortson[9], D. Gall[12], G. H. Gillanders[8], J. Grube[6], G. Gyuk[9], D. Hanna[10], E. Hays[1,14,15], M. Kertzman[16], J. Kildea[3], A. Konopelko[17], H. Krawczynski[5], F. Krennrich[18], M. J. Lang[8], K. Lee[5], P. Moriarty[2], T. Nagai[18], J. Niemiec[18,19], R. A. Ong[7], J. S. Perkins[3], M. Pohl[18], J. Quinn[6], P. T. Reynolds[20], H. J. Rose[4], G. H. Sembroski[12], A. W. Smith[1], D. Steele[9], S. P. Swordy[14], J. A. Toner[8], V. V. Vassiliev[7], S. P. Wakely[14], T. C. Weekes[3], R. J. White[4], D. A. Williams[21], M. D. Wood[7], B. Zitzer[12], H. D. Aller[22], M. F. Aller[22], M. Baker[23], D. Barnaby[24], M. T. Carini[24], P. Charlot[25,26], J. P. Dumm[23], N. E. Fields[23], T. Hovatta[27], B. Jordan[28], Y. A. Kovalev[29], Y. Y. Kovalev[29,30], H. A. Krimm[31,32], O. M. Kurtanidze[33], A. Lähteenmäki[27], J. F. Le Campion[25,26], J. Maune[24], T. Montaruli[23], A. C. Sadun[34], S. Smith[24], M. Tornikoski[27], M. Turunen[27], and R. Walters[24]

[1] High Energy Physics Division, Argonne National Laboratory, 9700 South Cass Avenue, Argonne, IL 60439, USA; deirdre.horan@gmail.com
[2] Department of Physical and Life Sciences, Galway-Mayo Institute of Technology, Dublin Road, Galway, Republic of Ireland
[3] Fred Lawrence Whipple Observatory, Harvard-Smithsonian Center for Astrophysics, P.O. Box 97, Amado, AZ 85645-0097, USA
[4] School of Physics and Astronomy, University of Leeds, Leeds, LS2 9JT, UK
[5] Department of Physics, Washington University, St. Louis, MO 63130, USA
[6] School of Physics, University College Dublin, Belfield, Dublin 4, Republic of Ireland
[7] Department of Physics and Astronomy, University of California, Los Angeles, CA 90095, USA
[8] School of Physics, National University of Ireland, Galway, Republic of Ireland
[9] Astronomy Department, Adler Planetarium and Astronomy Museum, Chicago, IL 60605, USA
[10] Physics Department, McGill University, Montréal, QC H3A 2T8, Canada
[11] Department of Astronomy and Astrophysics, 525 Davey Lab., Penn. State University, University Park, PA 16802, USA
[12] Department of Physics, Purdue University, West Lafayette, IN 47907, USA
[13] Department of Physics and Astronomy, Barnard College, Columbia University, NY 10027, USA
[14] Enrico Fermi Institute, University of Chicago, Chicago, IL 60637, USA
[15] NASA/Goddard Space-Flight Center, Code 661, Greenbelt, MD 20771, USA
[16] Department of Physics and Astronomy, DePauw University, Greencastle, IN 46135-0037, USA
[17] Physics Department, Pittsburg State University, 1701 South Broadway, Pittsburg, KS 66762, USA
[18] Department of Physics and Astronomy, Iowa State University, Ames, IA 50011, USA
[19] Instytut Fizyki Jądrowej PAN, ul. Radzikowskiego 152, 31-342 Kraków, Poland
[20] Department of Applied Physics and Instrumentation, Cork Institute of Technology, Bishopstown, Cork, Republic of Ireland
[21] Santa Cruz Institute for Particle Physics and Department of Physics, University of California, Santa Cruz, CA 95064, USA
[22] Department of Astronomy, University of Michigan, Ann Arbor, MI 48109-1042, USA
[23] University of Wisconsin, Madison, WI 53706, USA
[24] Western Kentucky University, 1 Big Red Way, Bowling Green, KY 42104, USA
[25] Université de Bordeaux, Observatoire Aquitain des Sciences de l'Univers, 2 rue de l'Observatoire, BP 89, 33271 Floirac Cedex, France
[26] CNRS, Laboratoire d'Astrophysique de Bordeaux-UMR 5804, 2 rue de l'Observatoire, BP 89, 33271 Floirac Cedex, France
[27] Metsähovi Radio Observatory, TKK, Helsinki University of Technology, Metsähovintie 114, 02540 Kylmälä, Finland
[28] School of Cosmic Physics, Dublin Institute For Advanced Studies, Dublin, Republic of Ireland
[29] Astro Space Center of Lebedev Physical Institute, Profsoyuznaya 84/32, 117997 Moscow, Russia
[30] Max-Planck-Institut für Radioastronomie, Auf dem Hügel 69, 53121 Bonn, Germany
[31] CRESST and NASA Goddard Space-Flight Center, Greenbelt, MD 20771, USA
[32] Universities Space Research Association, 10211 Wincopin Circle, Suite 500, Columbia, MD 21044-34342, USA
[33] Abastumani Observatory, 383762 Abastumani, Georgia
[34] Department of Physics, University of Colorado Denver, Denver, CO 80208, USA
Received 2008 July 15; accepted 2009 January 15; published 2009 March 31

ABSTRACT

Since 2005 September, the Whipple 10 m Gamma-ray Telescope has been operated primarily as a blazar monitor. The five northern hemisphere blazars that have already been detected at the Whipple Observatory, Markarian 421 (Mrk 421), H1426+428, Mrk 501, 1ES 1959+650, and 1ES 2344+514, are monitored routinely each night that they are visible. We report on the Mrk 421 observations taken from 2005 November to 2006 June in the gamma-ray, X-ray, optical, and radio bands. During this time, Mrk 421 was found to be variable at all wavelengths probed. Both the variability and the correlations among different energy regimes are studied in detail here. A tentative correlation, with large spread, was measured between the X-ray and gamma-ray bands, while no clear correlation was evident among the other energy bands. In addition to this, the well-sampled spectral energy distribution of Mrk 421 (1101+384) is presented for three different activity levels. The observations of the other blazar targets will be reported separately.

Key words: BL Lacertae objects: individual (Markarian 421) – gamma rays: observations – X-rays: individual (Markarian 421)
Online-only material: color figures

1. INTRODUCTION

Among active galactic nuclei (AGNs), blazars are the most extreme and powerful sources known and are believed to have their jets more aligned with the line of sight than any other class of radio-loud AGNs. They are high-luminosity objects, characterized by large, rapid, irregular amplitude variability in all accessible spectral bands. They have a core-dominated radio morphology with flat (α_r, $\propto \nu^{-\alpha_r} \lesssim 0.5$) radio spectra, which join smoothly to the infrared (IR), optical, and ultraviolet (UV) spectra. In all of these bands, the flux exhibits high and variable polarization. Blazars are visible across the entire electromagnetic spectrum having a broad continuum extending from the radio through the gamma-ray regime. Although much is known about the characteristics of their broadband emission, there are still many uncertainties about the underlying blazar emission mechanisms and many different models can explain their observed properties (Böttcher 2007; Sambruna 2007). Their high variability and broadband emission make long-term, well-sampled, multiwavelength (MWL) observations of blazars very important for constraining and understanding their emission mechanisms and characteristic timescales.

When plotted as νF_ν versus frequency, the blazar spectral energy distribution (SED) has a double-peaked structure. Both peaks are found to vary, often both in strength and in peak frequency, as the activity level of the blazar changes. The first peak is usually referred to as the synchrotron peak because in both leptonic and hadronic models for blazar emission, it is believed generally to be the result of incoherent synchrotron emission from relativistic electrons and positrons, presumed to be present in the magnetic fields of the jet. The origin of the second peak, usually referred to as the inverse-Compton peak, is less well determined. In synchrotron self-Compton (SSC) models, it is assumed that the synchrotron photons are up-scattered to higher energies by the electrons, while in external Compton (EC) models, these seed photons can come from the accretion disk, the broad-line region, the torus, the local IR background, the cosmic microwave background, the ambient photons from the central accretion flow or some combination of these sources. Hadronic models have also been invoked to explain the broadband spectra of blazars (e.g., Mannheim 1993; Mücke et al. 2003). Aharonian (2000) proposed that the X-ray to gamma-ray emission is synchrotron radiation from protons accelerated in highly magnetized compact regions of the jet. Other authors propose that proton–proton collisions, either within the jet itself or between the jet and ambient clouds, give rise to neutral pions which then decay to gamma rays (Dar & Laor 1997; Beall & Bednarek 1999; Pohl & Schlickeiser 2000).

As of this writing, 22 of the high-confidence sources in the rapidly growing catalog of very high energy (VHE; $E >$ 100 GeV) sources are AGNs.[35] All but one of these, the Fanaroff–Riley Type I galaxy M87, are blazars. Of the blazars, one is a flat spectrum radio quasar, three are low-frequency-peaked BL Lac objects, and the remainder are high-frequency-peaked BL Lac objects (HBLs). Five of the TeV blazars have been detected with the Whipple 10 m Gamma-ray Telescope. The VHE emission from four of these blazars was first discovered at the Whipple Observatory, which has been in operation with an imaging camera from 1982 until the present day (Kildea et al. 2007).

Imaging atmospheric Cherenkov telescopes (IACTs), such as the Whipple Telescope, have sufficient sensitivity to sample the short-term variability of blazars. However, IACT duty cycles are low (∼10%) because they can only operate on clear, moonless nights. Typically, less than 1000 hr per year are available for observing and therefore, the observing programs are oversubscribed. In 2005 September, the first telescopes of the VERITAS array (Weekes et al. 2001) came on line and the observing program at the Whipple Telescope was redefined to dedicate it almost exclusively to nightly blazar monitoring. Since that time, Markarian 421 (Mrk 421), H1426+428, Mrk 501, 1ES 1959+650, and 1ES 2344+514 have been monitored routinely each night that they are visible (dark clear skies, elevation $> 55°$, when possible). For the first time, this has provided the opportunity to obtain long-term and well-sampled VHE light curves of these highly variable objects. Part of the motivation for these observations was to provide a trigger for more sensitive VHE observations of these AGNs by the new generation of IACT telescopes (CANGAROO-III, HESS, MAGIC, and VERITAS) and to provide baseline observations for similar observations with *GLAST*.

The results of the monitoring campaign on Mrk 421 (1101+384) are described here. At a redshift of $z = 0.031$, Mrk 421 was the first source of VHE gamma rays to be discovered (Punch et al. 1992). Since that pivotal discovery, Mrk 421 has been studied extensively in the VHE band and many periods of intense variability have been observed. Mrk 421 is the archetypal HBL. Historically, it has exhibited shifts in both the peak frequency and in the power of the first and second components of the SED (Fossati et al. 2008). In 2001 April, Mrk 421 entered an extremely active phase. It was observed intensively with the Whipple 10 m Telescope during this time and, for the first time in an HBL, the spectrum in the VHE regime was found to harden as the flux of VHE gamma rays increased (Krennrich et al. 2002; Fossati et al. 2008).

Often, for MWL campaigns in which VHE telescopes participate, the call for full MWL coverage is invoked when large flares are observed in the TeV band (Krawczynski et al. 2000, 2004; Rebillot et al. 2006; Fossati et al. 2008). Like the observations described here, the campaign carried out by Błażejowski et al. (2005) in 2003–2004 was not instigated due to flaring activity from Mrk 421. That campaign, which concentrated mainly on the X-ray and gamma-ray data, revealed the correlation between the emission in the two wavebands to be fairly loose. Rapid variability was detected in both wavebands, and the X-ray emission was found to peak days after the gamma-ray emission for one giant flare. Evidence for TeV orphan flaring, similar to that found in 1ES 1959+650 by Krawczynski et al. (2004), was also seen. In addition to significant X-ray and gamma-ray coverage, the data set described here includes excellent coverage of Mrk 421 in the optical and radio bands.

To encourage and coordinate observations of the target AGN at other wavelengths, a Web site containing the observing timetable and the preliminary light curves at TeV wavelengths was made publicly accessible and continuously maintained via the Whipple link on the VERITAS Web site: http://veritas.sao.arizona.edu. E-mails were distributed throughout 2005–2006 to coordinate the Mrk 421 observations. Data from 12 different wavebands, spanning more than 18 orders of magnitude in energy, were obtained over a period of approximately 230 days. Because this campaign was not triggered by activity at any wavelength, there were no a priori assumptions about flux levels and we can look for correlations on longer

[35] http://tevcat.uchicago.edu

Table 1
The Mrk 421 Data Set Presented in this Paper

Waveband	Instrument	Energy Range (eV)	No. of Data Points	MJD Range
Radio	RATAN 1 GHz	$3.7–4.6 \times 10^{-6}$	2	53821 and 53890
	RATAN 2.3 GHz	$8.6–10.5 \times 10^{-6}$	2	53821 and 53890
	RATAN 4.8 GHz	$1.8–2.2 \times 10^{-5}$	2	53821 and 53890
	UMRAO 4.8 GHz	$1.8–2.2 \times 10^{-5}$	12	53706–53918
	RATAN 8 GHz	$3.0–3.6 \times 10^{-5}$	2	53821 and 53890
	UMRAO 8 GHz	$3.0–3.6 \times 10^{-5}$	16	53650–53899
	RATAN 11 GHz	$4.1–5.0 \times 10^{-5}$	2	53821 and 53890
	UMRAO 14.5 GHz	$5.2–6.8 \times 10^{-5}$	22	53664–53907
	VLBA 15 GHz	$5.6–6.8 \times 10^{-5}$	1	53830
	RATAN 22 GHz	$8.2–10.0 \times 10^{-5}$	2	53821 and 53890
	Metsähovi 37 GHz	$1.5–1.6 \times 10^{-4}$	31	53650 and 53905
Optical	Abastumani	1.7–2.3	31	53801–53896
	Bell	1.8–2.2	19	53824–53909
	Bradford	1.7–2.2	35	53771–53922
	FLWO	1.8–2.3	64	53663–53898
	Tenagra	1.7–2.2	13	53726–53876
	Torini	1.7–2.3	4	53757–53838
	Bordeaux	2.1–2.5	9	53819–53861
	Bradford	2.1–2.5	36	53771–53922
	Tenagra	2.1–2.5	13	53726–53876
	WIYN	2.1–2.5	19	53842–53872
	Bradford	2.7–3.2	31	53771–53896
	Tenagra	2.6–3.2	13	53726–53876
	WIYN	2.6–3.3	19	53842–53872
X-ray	XRT	$0.2–10 \times 10^{3}$	24	53737–53914
	ASM	$2–10 \times 10^{3}$	256	53670–53930
	PCA	$3–25 \times 10^{3}$	75	53741–53887
	BAT	$15–50 \times 10^{3}$	234	53670–53931
Gamma-ray	Whipple	$0.2–10 \times 10^{12}$	80	53676–53908

timescales and under different source conditions. Since these Mrk 421 data were gathered over a long period of time and, in the case of some wavebands, from a number of different instruments for a particular energy range, it was important to ensure that the data were well calibrated so that the variability of Mrk 421 over the course of the campaign was not contaminated by inaccurate intra-night and/or intra-telescope normalizations.

In Section 2, we describe the observations presented in this paper. This section is subdivided by wavelength band. In Section 3 the results of the observations are presented, while in Section 4 we discuss the implications of these results in the context of emission models.

2. OBSERVATIONS AND DATA REDUCTION

The complete data set presented in this paper is summarized in Table 1 and the light curves are shown together in Figure 1. In the following section, the data collection procedures and the Mrk 421 data gathered at each of the instruments are described.

2.1. VHE Gamma-ray Data

All the TeV gamma-ray observations presented here were made with the 10 m Gamma-ray Telescope at the Fred Lawrence Whipple Observatory (FLWO; Kildea et al. 2007). Although sensitive in the energy range from 200 GeV to 20 TeV, the peak response energy of the telescope to a Crab-like spectrum during the observations reported upon here was approximately 400 GeV. This is the energy at which the telescope is most efficient at detecting gamma rays and, as is typical for IACTs such as Whipple, is subject to a 20% uncertainty.

The Mrk 421 data were analyzed using the imaging technique and analysis procedures developed by the Whipple Collaboration (Hillas 1985; Reynolds et al. 1993). A Quicklook analysis was performed at the conclusion of each observation and the results were posted daily on a public Web site.[36] Three offline analyses (independent but using the standard Supercuts methodology) were used to derive the TeV light curves presented here.

Two different modes of observation are employed at the Whipple Telescope, "*On–Off*" and "*Tracking*" (Catanese et al. 1998). In both modes, the data are usually taken in 28 minute scans. Unlike data taken in the *On–Off* mode, the scans taken in the *Tracking* mode do not have independent control data which can be used to establish the background level of gamma-ray like events during the scan. These control data are essential in order to estimate the number of events passing all cuts that would have been detected during the scan in the absence of the candidate gamma-ray source. In order to perform this estimate, a tracking ratio is calculated by analyzing "darkfield data" (Horan et al. 2002). These consist of *Off-Source* data taken in the *On–Off* mode and of observations of objects found not to be sources of gamma rays. A large database of these scans is analyzed and, in this way, the background level of events passing all gamma-ray selection criteria can be characterized as a function of zenith angle. The data presented here were mostly taken in the *Tracking* mode.

During the period MJD 53676 to MJD 53908, a total of 144.1 hr of data were taken on Mrk 421. Since IACTs can only operate during moonless conditions, there is a period centered on full moon each month when gamma-ray observations are not possible. From the total of 328 runs on the source (*On* and *Tracking* modes), 275 runs (84%), comprising 122.57 hr, survived the quality selection process. Apart from any problems reported by observers in the nightly logs, the main parameter used to determine whether the data run should be included in the final analysis was the stability of the raw trigger rate. Any data run whose raw trigger rate deviated significantly from being steady for its duration was discarded.

When possible, the AGN data were interspersed with observations of the Crab Nebula, the standard candle in this energy regime. A total of 44.41 hr of these were taken and subjected to the same analysis procedure. In addition, nightly runs were taken with the telescope pointing to the zenith; these data were used to calculate the telescope throughput (Lebohec & Holder 2003) so that data could be corrected for inter-nightly changes in atmospheric transparency. Both the AGN and the Crab data were corrected for variations in the throughput. In addition to this, a correction was applied to compensate for elevation effects in the data due to the increasing volume of atmosphere through which the Cherenkov light propagates as the zenith angle of the observations increases. These corrections ensured that data taken on different nights, under different atmospheric conditions and at different elevations could be compared. The Mrk 421 rates were then converted into equivalent Crab rates. It should be noted that this simplistic scaling is strictly only valid for a TeV spectrum near that of the Crab Nebula (spectral index of −2.6). Although Mrk 421 has been known to display spectral variability in the past, the measurement uncertainties on the flux points are such that the effect of spectral variability should not be significant. The gamma-ray light curve containing the rate from each approximately 28 minute scan on Mrk 421 is shown in Figure 2.

[36] http://veritas.sao.arizona.edu/content/blogsection/6/40

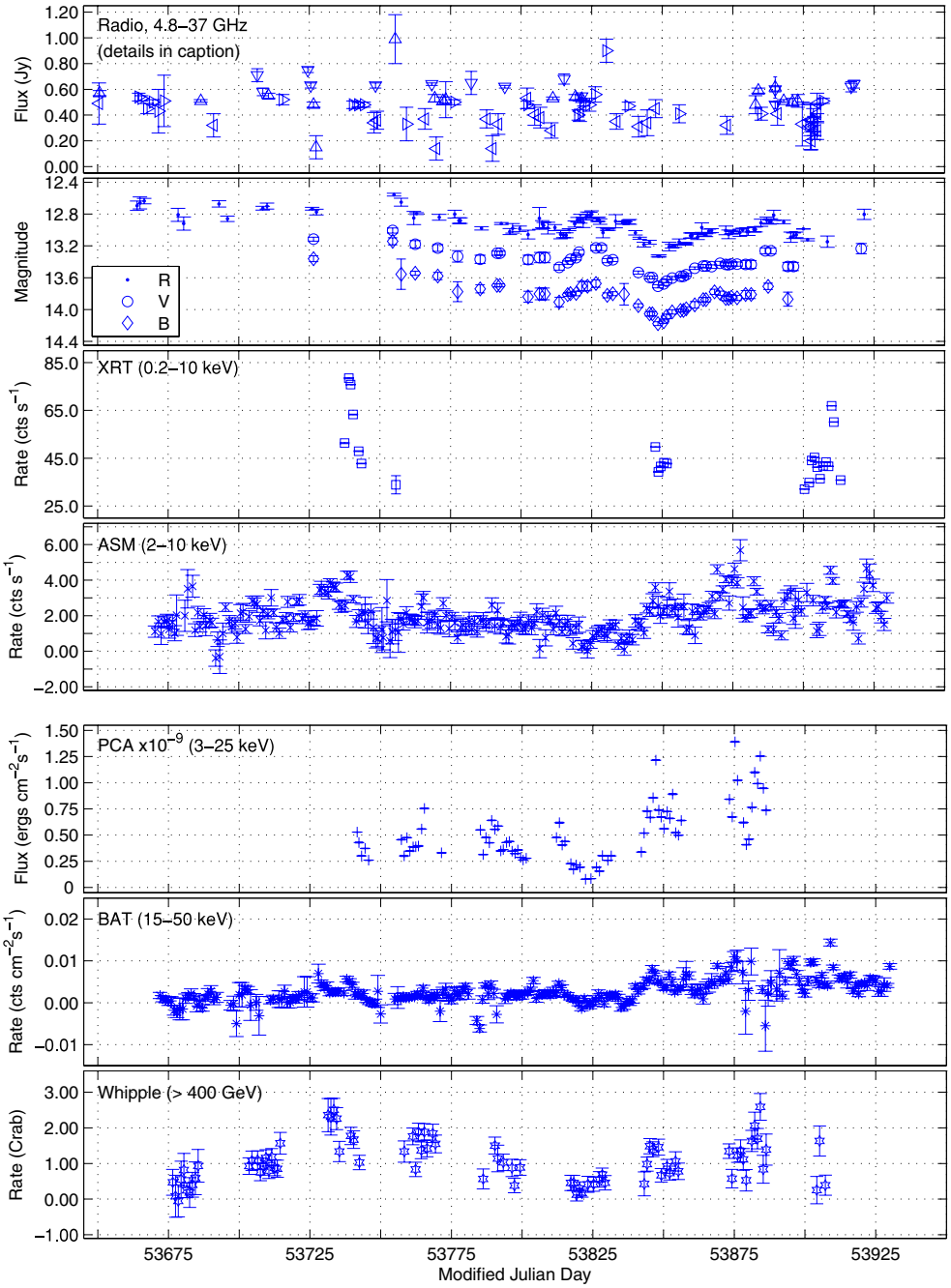

Figure 1. Entire database, as summarized in Table 1. Each data point represents all data obtained on that night as part of this campaign. The radio data at four different frequencies are plotted in the top panel: 4.8 GHz (▽), 8 GHz (△), 14.5 GHz (▷), and 37 GHz (◁). The optical data are combined from many different observatories (Table 2).

(A color version of this figure is available in the online journal.)

2.2. X-ray Data

The X-ray data for this MWL campaign span the energy range from 0.2 to 50 keV. These data come from four different instruments, two on the *Rossi X-ray Timing Explorer* (*RXTE*) and two on the *Swift* satellite. The X-ray light curves are shown together with the gamma-ray data in Figure 3. The details of the analysis of each X-ray data set are given in the following subsections.

2.2.1. The All Sky Monitor (ASM)

The ASM, on board the *RXTE* (Bradt et al. 1993) operates in the 1.5–12 keV energy band and scans most of the sky every 1.5 hr. It consists of three coded aperture cameras, scanning shadow cameras, which can be rotated to view different regions of the sky (Levine et al. 1996). Each scanning shadow camera is a sealed proportional counter filled with a xenon–CO_2 mixture. The data presented here are the 1-day averages from the ASM quicklook pages.[37] Each 1-day average data point represents the 1-day average of the fitted source fluxes from a number (typically 5–10) of individual ASM dwells. A total of 256 nights of ASM data on Mrk 421 are presented here from MJD 53670 to MJD 53930. During this time, the mean nightly flux from Mrk 421 in the 2–10 keV band was 1.99 counts s^{-1}.

[37] http://http://xte.mit.edu/XTE

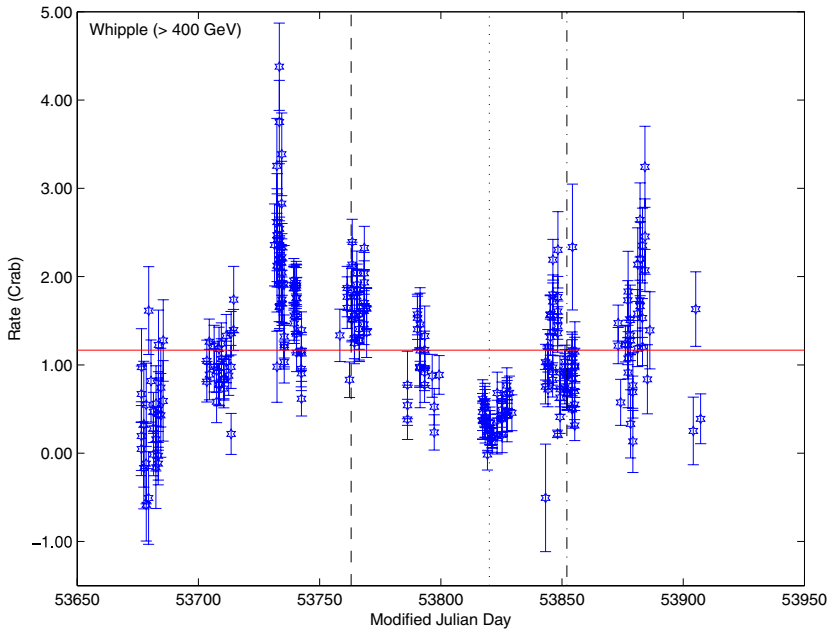

Figure 2. Gamma-ray light curve, with each exposure (typically 28 minute) binned separately, for the duration of the observing campaign. The nights for which the SED was calculated are marked: low state by the dotted line; medium state by the dash-dotted line; high state by the dashed line. The horizontal red line shows the mean rate detected during a single exposure on Mrk 421.

(A color version of this figure is available in the online journal.)

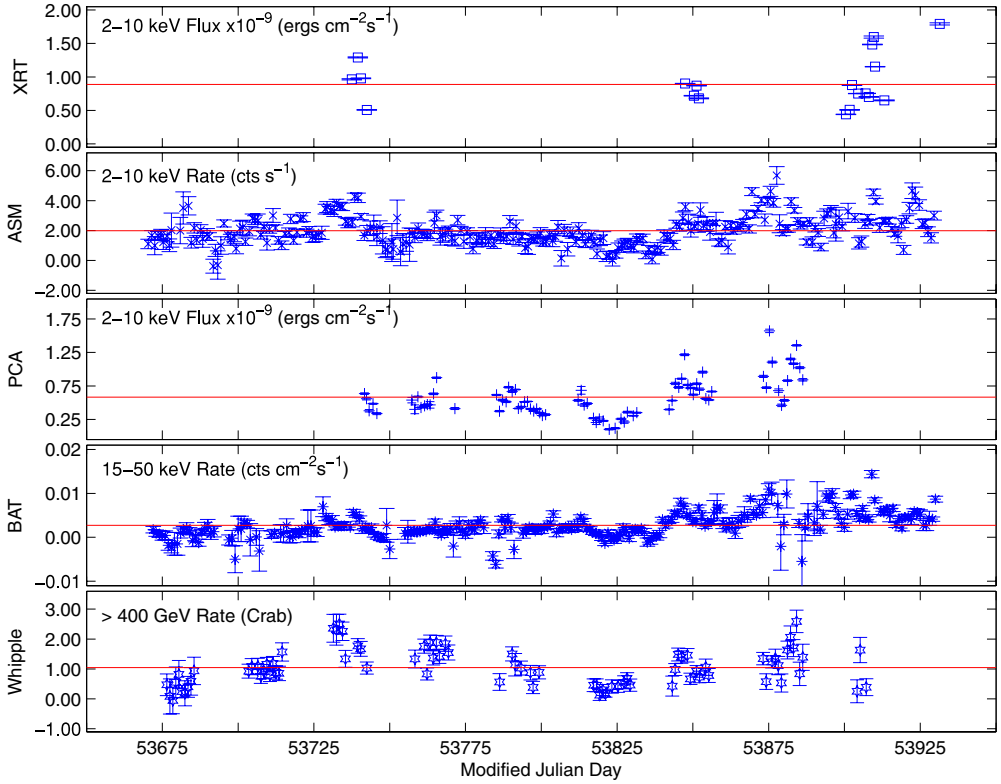

Figure 3. X-ray and gamma-ray light curves. The mean flux in each waveband is shown by a horizontal red line. Top: XRT; 2nd from top: ASM; middle: PCA; 2nd from bottom: BAT; bottom: gamma ray. Each data point represents all data obtained on that night as part of this campaign.

(A color version of this figure is available in the online journal.)

2.2.2. The Proportional Counter Array (PCA)

The primary instrument on board NASA's X-ray satellite *RXTE* is the PCA. It is an array of five proportional counters with a total net area of 6250 cm^2 and is effective over the energy range 2–60 keV. Mrk 421 was observed with the *RXTE* PCA from MJD 53741 to MJD 53887 in short daily exposures ranging from 2.1 to 48.0 minutes, with a mean exposure of 19 minutes. The PCA exposures were scheduled to coincide with the Whipple 10 m Telescope observations, so that the data gaps of ≈12 days in the X-ray database coincide with

Table 2
Participating Optical Observatories and Instruments, Camera Type, Filter System, Number of Nightly Data Points Contributed per Filter, and the Range of Dates Where Observing Took Place

Observatory	Camera	Filter System	No. of Nights			MJD Range
			R	*V*	*B*	
Abastumani 0.7 m	ST-6	Cousins	31			53801–53896
Bell 0.6 m	Appogee AP2P	Bessel	19			53824–53909
Bordeaux	Th7896M	GC495+BG38		9		53819–53861
Bradford 0.36 m	FLI MaxCam ME2	Johnson	35	36	31	53771–53922[a]
FLWO 1.2 m	Keplercam	SDSS	64[b]			53663[c]–53898
Tenagra 0.8 m	SITe based	Johnson/Cousins	13	13	13	53726–53876
Torino 1.05 m	Loral CCD	Cousins	4			53757–53838
WIYN 0.9 m	S2KB	Harris		19	19	53842–53872

Notes. Some information is unavailable for the Bradford and Bordeaux Observatories. For the FLWO 1.2 m, the filter system is "SDSS" for Sloan Digital Sky Survey.
[a] The *B*-band data from Bradford were taken between MJDs 53771 and 53896.
[b] These data were taken in the *R* band.
[c] Data-taking on Mrk 421 at FLWO began before the gamma-ray data-taking.

the bright moon periods when no gamma-ray observations were possible. Due to various observing constraints, the X-ray and gamma-ray observations were not always simultaneous, with the PCA observations starting on average 99 minutes behind the Whipple 10 m observations. Data analysis was carried out with the HEAsoft 6.1 tools and current calibration files, following the standard procedure. The version number is consistent with the *Swift* analysis. The PCA data presented here comprise 75 exposures from MJD 53741 to MJD 53887 with a mean flux of 5.18×10^{-10} erg cm^{-2} s^{-1}.

2.2.3. The X-ray Telescope (XRT)

The XRT, one of the instruments on the *Swift* satellite (Gehrels et al. 2004), is a focusing XRT with a 110 cm^2 effective area and a 23 arcmin field of view (Burrows et al. 2005). It is sensitive to X-rays in the 0.2–10 keV band. The XRT data presented here were reduced using the latest HEAsoft tools (ver. 6.1.0), including *Swift* software version 2.0, and the latest response (ver. 8) and ancillary response files (created using *xrtmkarf*) available in CALDB at the time of analysis. Data were screened with the standard parameters, including the elimination of time periods when the CCD temperature was warmer than $-48\,^{\circ}$C. Due to the high rates of Mrk 421 during the XRT observations, only Windowed Timing (WT) mode data were used in this analysis, and only grades 0–2 were included. Since the count rate stayed below $\approx$100 counts s^{-1}, the WT mode data is free of significant pile-up effects. The data were corrected for effects due to bad columns and bad pixels. Source and background regions were both chosen in a way that avoids overlap with serendipitous sources in the image.

For the analysis presented here, data from the XRT were summed in 1-day bins resulting in a total of 24 measurements from MJD 53737 to MJD 53913. As can be seen in Figure 3, the XRT light curve is the most sparsely sampled of the X-ray light curves. During all XRT observations reported on here however, Mrk 421 was detected above 5σ. The mean flux from Mrk 421 during these XRT observations in the energy range from 0.2 to 10 keV was 47.23 counts s^{-1}.

2.2.4. The Burst Alert Telescope (BAT)

The BAT (Barthelmy et al. 2000), also on the *Swift*, is a large field of view (1.4 sr) XRT with imaging capabilities in the energy range from 15 to 150 keV. It has a coded aperture mask with 0.52 m^2 CdZnTe detectors. The BAT typically observes 50%–80% of the sky each day and has accumulated light curves for 530 non-gamma-ray burst (non-GRB) sources (Krimm 2006). The BAT data shown here are the *Swift*/BAT transient monitor results provided by the *Swift*/BAT team (Krimm 2008a) and span the energy range from 15 to 50 keV. As part of its on-board GRB monitor, the BAT flight software produces "scaled maps" in the energy band 15–50 keV and on timescales $\geqslant$64 s. The data were first verified to ensure that any corrupted or incomplete data were rejected. Then, they were analyzed using the standard BAT software tools. Full details of this analysis are given at the BAT transients Web site (Krimm 2008b). BAT data are available for 240 nights during this MWL campaign. When these were filtered to remove data that were flagged as bad, 234 nights remained. These data were taken between MJDs 53670 and 53930 and, during this time, the mean flux from Mrk 421 recorded by the BAT in the energy range from 15 to 50 keV was 2.72×10^{-3} counts s^{-1}.

2.3. Optical Data

Eight optical observatories contributed data sets to this campaign. They are the FLWO 1.2 m telescope (located adjacent to the Whipple 10 m Gamma-ray Telescope on Mt. Hopkins), the Tenagra 0.8 m telescope in Tenagra, Arizona, USA, the Bradford Robotic Telescope in Tenerife, Canary Islands, Spain, the WIYN 0.9 m telescope on Kitt Peak, Arizona, USA, the 0.7 m telescope at Abastumani Observatory in Abastumani, Georgia, the 0.6 m Bell Observatory at Western Kentucky University, USA, Bordeaux Observatory in Floriac, France, and the 1.05 m REOSC telescope at Osservatorio Astronomico di Torino, Italy. Table 2 gives a brief description of each telescope, its filter system and bandpass, and its contribution to the optical data set.

The data from the various observatories were reduced and the photometry performed independently by different analysts using different strategies. The FLWO, Bradford, and Tenagra data, for example, usually consisted of a single or a few images per filter per night. Relative aperture photometry was performed using standard routines in IRAF.[38] Magnitudes were calculated

[38] IRAF is distributed by the National Optical Astronomy Observatory, which is operated by the Association of Universities for Research in Astronomy, Inc., under cooperative agreement with the National Science Foundation. http://iraf.noao.edu/

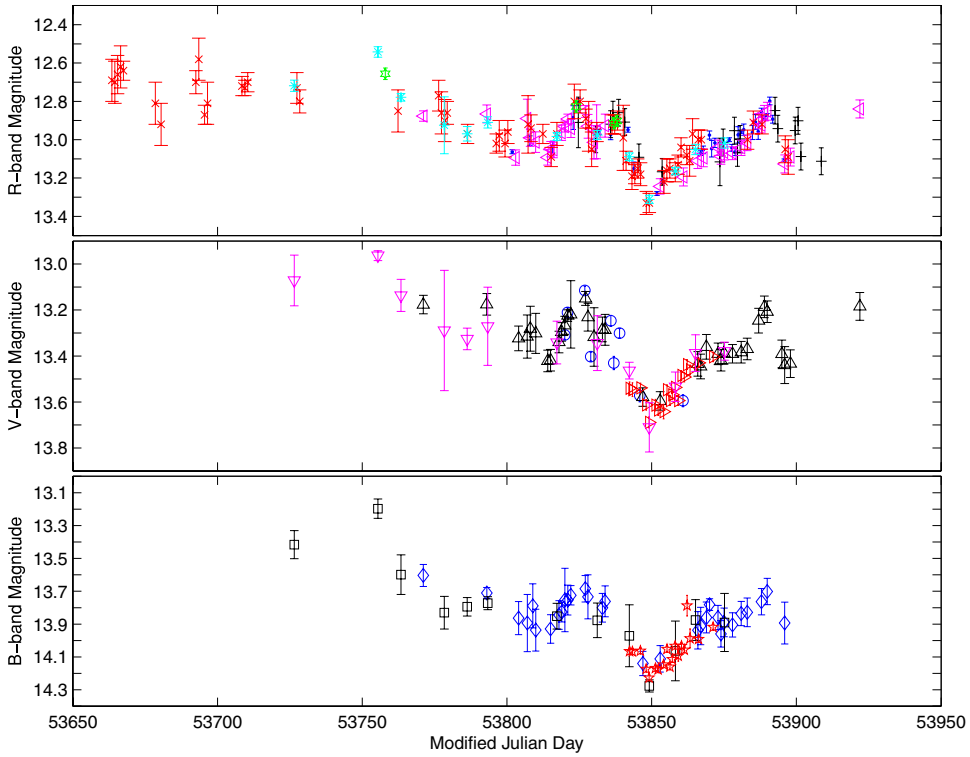

Figure 4. Top: Composite *R*-band light curve with the following legend—Abastamani: blue dots; Bell: black plus symbols; Bradford: magenta ◁ symbols; FLWO: red × symbols; Tenagra: cyan asterisks; Torini: green hexagrams. Middle: Composite *V*-band light curve with the following legend—Bordeaux: blue circle; Bradford: black △ symbols; WIYN: red ▷ symbols; Tenagra: magenta ▽ symbols. Bottom: Composite *B*-band light curve with the following legend—Bradford: blue diamonds; Tenagra: black squares; WIYN: red pentagrams.

(A color version of this figure is available in the online journal.)

with respect to star 1 of Villata (Villata et al. 1998) with a photometry aperture of 10 arcsec. The host galaxy light was not subtracted at this stage of the analysis. Other optical analysts used slightly different strategies: the photometry for the Bell, WIYN, and Abastumani data were quoted with respect to stars 1–3 of Villata, and the Torino photometry was performed using Gaussian fitting rather than by counting within a fixed aperture.

Combining the various optical data to produce a composite light curve for each spectral band is complicated by the fact that different observatories use different photometric systems. Furthermore, photometric apertures and the definition of the reported measurement error for each nightly averaged flux is inconsistent across data sets. Therefore, we have adopted a simple approach for the construction of the composite light curves whereby a unique flux offset is found for each spectral band of every instrument based on overlapping observations (Steele et al. 2008).

In the *R* band, for example, we first find the initial average flux offset for each *R*-band light curve with respect to that of the FLWO (since it spans the largest range of dates) based on observations overlapping by less than 0.8 days (except for the Bell and Torino light curves, whose coincidence windows were widened to 1.8 days to ensure a sufficient number of overlaps). Then, for each light curve, a comparison light curve is constructed using the light curves from the other observatories with the initial flux offsets applied. A new offset is then found for each light curve based on overlapping observations in the respective comparison light curve. The process is repeated iteratively until the variance of the offset residuals for each light curve is minimized. The final composite light curve for each spectral band is then made by simply combining the nightly averaged flux from each observatory with the final offsets applied and these are shown in Figure 4. Of the three wavelengths, the *R* band is the best sampled, comprising 166 data points on 97 nights spanning a period of 260 days. Figure 5 shows the very well-sampled optical light curves, after all the data from different instruments have been combined and normalized, along with the gamma-ray data during this campaign. The mean magnitude of Mrk 421 during this campaign was 12.95 in the *R* band, 13.40 in the *V* band, and 13.82 in the *B* band.

2.4. Radio

Typically, the variations in AGN are slower at radio frequencies than at the higher frequency bands with the most variability being observed at the higher radio frequencies (see, e.g., Kovalev et al. 2002). In general, because of this slower long-term variability, AGNs are not observed with as high temporal coverage in this regime. The radio data presented here were taken at eight frequencies at three different radio observatories but, for four of these frequency bands the radio coverage was very sparse. The fluxes and their associated standard errors are given in janskys, so they have already been normalized for the bandwidth of their receivers. Generally, Mrk 421 is found to vary on monthly timescales. The radio light curves are shown along with the gamma-ray light curve in Figure 6. In the subsections that follow, the radio data and analysis from the participating observatories are described.

2.4.1. Metsähovi Radio Observatory

The 37 GHz observations were made with the 13.7 m diameter Metsähovi radio telescope, which is a radome

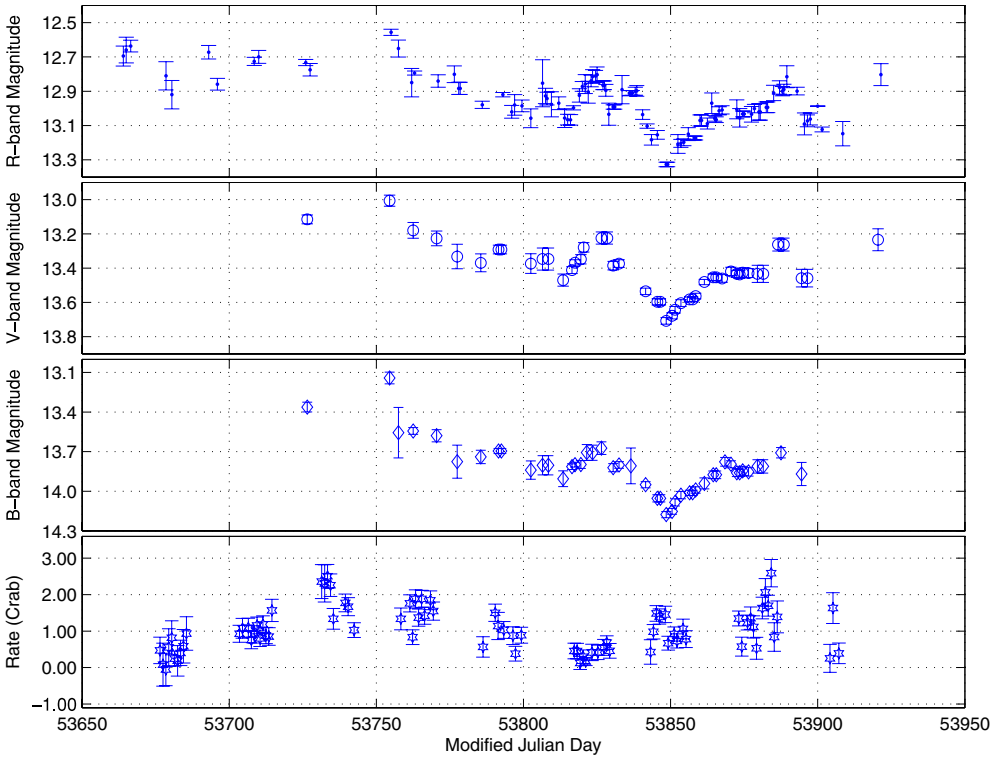

Figure 5. Normalized optical light curves and the gamma-ray light curve. The data were binned by MJD—top: *R* band; second from top: *V* band; second from bottom: *B* band; bottom: gamma ray.

(A color version of this figure is available in the online journal.)

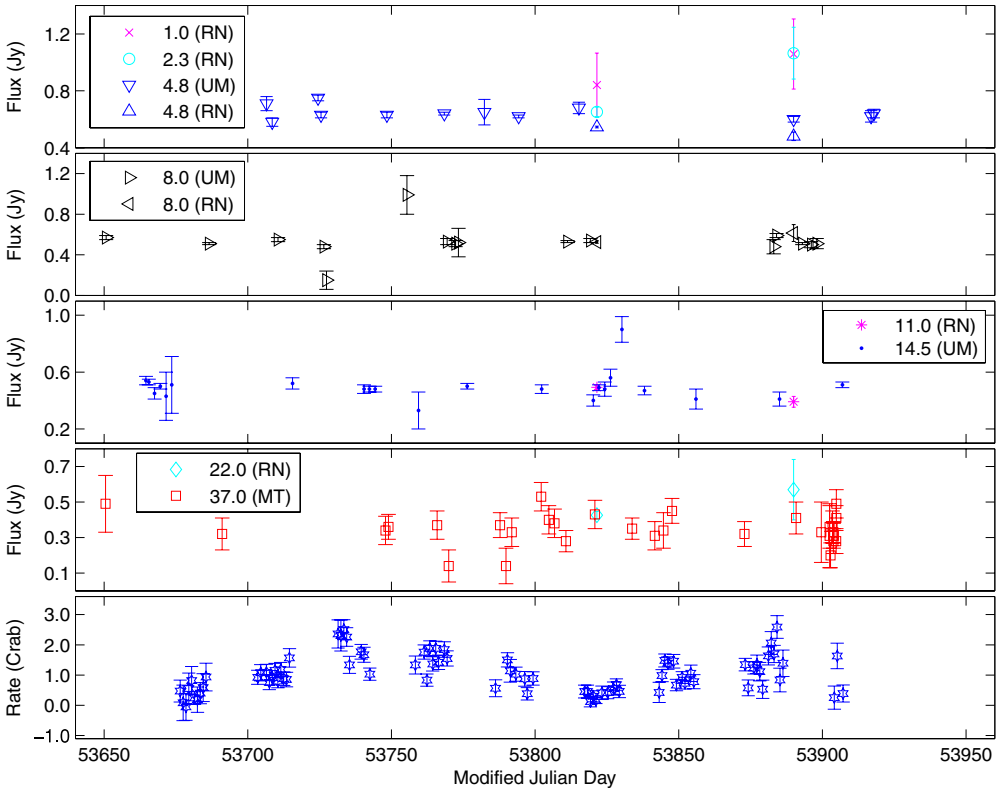

Figure 6. All of the radio data taken during this observing campaign. Top: the data from 1.0 to 4.8 GHz from RATAN (RN) and the UMRAO (UM); second from top: the data at 8.0 GHz from RATAN (RN) and the UMRAO (UM); middle: the data from 11.0 to 14.5 GHz from RATAN (RN) and the UMRAO (UM); second from bottom: the data from 22.0 to 37.0 GHz from RATAN (RN) and Metsähovi (MT). Bottom: the gamma-ray data from the Whipple 10 m Telescope. Each data point represents all data obtained on that night as part of this campaign.

(A color version of this figure is available in the online journal.)

enclosed paraboloid antenna situated in Finland (2423′38″E, +6013′05″). The measurements were made with a 1 GHz band dual beam receiver centered at 36.8 GHz. The high electron mobility pseudomorphic transistor (HEMPT) front end operates at room temperature. The observations are ON–ON observations, alternating the source and the sky in each feed horn. A typical integration time to obtain one flux density data point is 1200–1400 s. The detection limit of the telescope at 37 GHz is on the order of 0.2 Jy under optimal conditions. Data points with a signal-to-noise ratio <4 are handled as nondetections.

The flux density scale is set by observations of DR 21. Sources 3C 84 and 3C 274 are used as secondary calibrators. A detailed description on the data reduction and analysis is given in Teräsranta et al. (1998). The error estimate in the flux density includes the contribution from the measurement rms and the uncertainty of the absolute calibration.

2.4.2. University of Michigan Radio Astronomy Observatory

Most of the data at 4.8, 8.0, and 14.5 GHz came from the University of Michigan Radio Astronomy Observatory (UMRAO) using the 26 m diameter parabolic reflector. Both on-source and background flux measurements were performed. To provide improved sensitivity, the receivers have relatively broad bandwidth of 500, 780, and 2000 MHz at the three frequencies, respectively. The adopted flux density scale is based upon the flux of Cassiopeia A, the primary flux calibrator, using its measured decay rate at centimeter wavelengths. A grid of secondary flux calibrators distributed in R.A. are also observed. In order to correct for environmental variations, a calibration source was observed approximately every 1–2 hr. The integration times at UMRAO are typically 30 minutes and measurements are usually taken within ±2.5 hr of the meridian.

2.4.3. Radio Astronomical Telescope of the Academy of Sciences

The 1–22 GHz instantaneous radio spectrum of Mrk 421 was observed with the 600 m ring radio telescope RATAN-600 (Korolkov & Parijskij 1979) of the Special Astrophysical Observatory, Russian Academy of Sciences, located in Zelenchukskaya, Russia, on 2006 March 26, 27, and 28, and 2006 May 3 and 4. The continuum spectrum was measured every time quasi-simultaneously (within several minutes) in a transit mode at six different bands with the following central frequencies (and bandwidths): 0.95 GHz (0.03 GHz), 2.3 GHz (0.25 GHz), 4.8 GHz (0.6 GHz), 7.7 GHz (1.0 GHz), 11.2 GHz (1.4 GHz), and 21.7 GHz (2.5 GHz). Details on the method of observation, data processing, and amplitude calibration are described in Kovalev et al. (1999). The March data were collected using the Northern sector of the telescope while the June spectrum was observed at the Southern sector with the Flat reflector. Since no significant time variations were found during three days in March and two days in May, two averaged RATAN total flux density spectra for 2006 March and May are provided and used in this paper.

2.4.4. VLBA: MOJAVE Program

In addition to these radio light curves, the data from the 2 cm Very Long Baseline Array (VLBA)/MOJAVE monitoring program (Kellermann et al. 2004; Lister & Homan 2005) for the epoch 2006 April 5 (MJD 53830) were used (see the 15 GHz VLBA image in Figure 7). The total flux density (Stokes I) at 15 GHz integrated over this image is 336 mJy. The flux density from the core region, when it is modeled using a circular Gaussian, is 288 mJy so Mrk 421 was very core dominated at this time implying that the bulk of the radio-band variability is associated with the VLBI-imaged core. The angular size of the modeled core on the half power level is 0.046 mas. The core size resolution limit was estimated for this data set following (Kovalev et al. 2005) and appeared to be less than the measured core size value. The linearly polarized flux density is 6 mJy. This polarized flux is detected from the core region only. VLBI core brightness temperature in the source frame is estimated to be 8×10^{11} K.

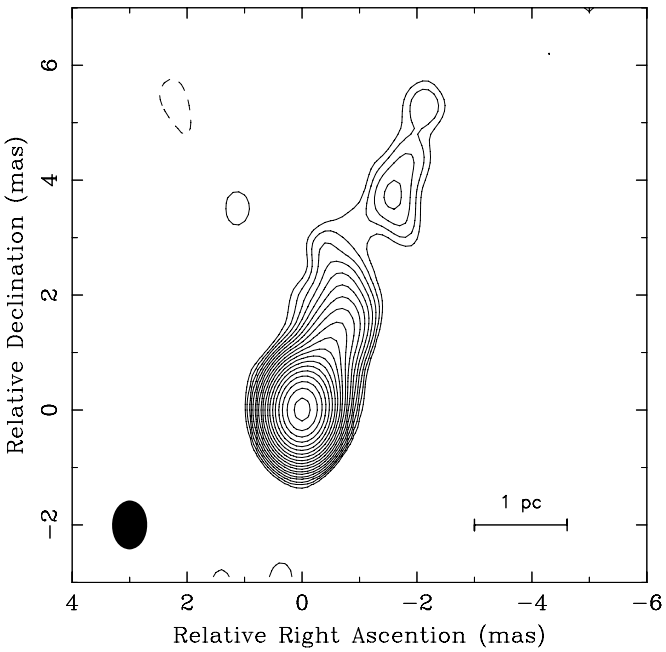

Figure 7. Naturally weighted VLBA Stokes I 15.3 GHz image of Mrk 421. The epoch of observation is 2006 April 5 (MJD 53830). The contours are plotted in successive powers of $\sqrt{2}$ times the lowest contour of 0.5 mJy. The peak intensity is 296 mJy beam^{-1}, the synthesized beam is shown in the left corner. This plot is made from an image FITS file provided by the 2 cm survey/MOJAVE programs database (Kellermann et al. 2004; Lister & Homan 2005).

3. RESULTS

The large, well-sampled MWL light curves collected on Mrk 421 during 2005–2006 enabled us to carry out a number of different analyses, which are described in the following subsections. The variability across the entire spectrum was investigated by computing both the fractional rms variability amplitude and the point-to-point fractional variability amplitude for each of the 12 wavebands. For the better-sampled light curves, namely those in the optical, X-ray and gamma-ray wavebands, a more detailed variability analysis was undertaken. Correlations were sought between the emission at different energies and the discrete correlation function (DCF) was computed for the optical-gamma and the X-ray-gamma data sets. Three different nights were chosen, when Mrk 421 was deemed to be in a high, medium and low emission state, and broadband SEDs were constructed for each of these nights. The high-flux SED was compared with those from archival Mrk 421 observations.

3.1. Variability Amplitude

The fractional rms variability amplitude, $F_{\rm var}$, and the point-to-point fractional rms variability amplitude, F_{pp} (Zhang et al.

2005), were calculated for each of the energy bands where a significant amount of data were gathered. They are defined as

$$F_{\rm var} = \sqrt{\frac{S^2 - \overline{\sigma^2}}{\bar{F}^2}} \quad (1)$$

and

$$F_{pp} = \frac{1}{\bar{F}} \sqrt{\frac{1}{2(N-1)} \sum_{i=1}^{N-1} (F_{i+1} - F_i)^2 - \overline{\sigma^2}}, \quad (2)$$

where each flux measurement F_i has a measurement error σ_i, $\bar{F}$ is the arithmetic mean of the counts, and

$$S^2 = \frac{1}{N-1} \sum_{i=1}^{N} (F_i - \bar{F})^2,$$

and $\overline{\sigma^2}$ is the mean error squared:

$$\overline{\sigma^2} = \frac{1}{N} \sum_{i=1}^{N} \sigma_i^2.$$

These quantities were calculated using 1-day binning for each of the data sets. These results can be seen for all wavebands apart from the 37 GHz radio data set in Table 3. For the 37 GHz data, the difference between the terms to be subtracted in both Equations (1) and (2) was negative, indicating that the measurement errors were larger than the variability observed, and therefore the calculation could not be completed. The fractional rms variability amplitude, $F_{\rm var}$, quantifies the integrated level of variability present in a particular waveband, while the point-to-point fractional rms variability amplitude, F_{pp}, probes the short-timescale variability by measuring the variations between adjacent points in the light curve. Their ratio, taken as a function of energy, provides information on the dependence of the power spectral density slope on energy (Zhang et al. 2005). Figure 8 shows $F_{\rm var}$ and the ratio of $F_{\rm var}$ to F_{pp} for 10 of the 12 wavebands. The values for the BAT data are not plotted because, as will be discussed in Section 4, the significance level of the BAT detection was less than 3σ on most nights ($\sim$58%) during this campaign.

3.2. Gamma-ray Flux Variability

Throughout the observations presented here, the gamma-ray rate from Mrk 421 was found to be variable. This is evident from the light curves shown in Figure 9, in which the average nightly gamma-ray rate is shown, and in Figure 2, where the gamma-ray rate is plotted for each observing scan (typically of 28 minute duration). Mrk 421 was observed by the TACTIC Gamma-ray Telescope (Yadov et al. 2007) during a time period overlapping with these Whipple observations and, although the energy ranges and sensitivities of the two instruments are slightly different, similar overall trends are present in the two data sets. The maximum gamma-ray rate for one of the Whipple 28 minute exposures occurred on MJD 53733 when a rate of 4.38 $\pm$ 0.49 Crab was recorded. This is a factor of 3.74 increase over the mean rate for a 28 minute exposure during this campaign. The light curve for MJD 53733 is shown in Figure 9. The mean gamma-ray rate for this night was the second highest recorded during this campaign at 2.50 $\pm$ 0.32 Crab. The flux from Mrk 421 can be seen to vary throughout this night, starting off at 1.91 $\pm$ 0.42 Crab before reaching its peak value and then decreasing to 1.67 $\pm$ 0.26 Crab. The maximum average nightly gamma-ray rate of 2.59 $\pm$ 0.37 Crab, a factor of 2.49 higher than the mean nightly rate, was recorded on MJD 53884. A summary of the mean, minimum, and maximum gamma-ray rate from Mrk 421 during this campaign is given in Table 3. The fractional rms variability amplitude in the gamma-ray band was found to be 0.511 with a point-to-point fractional rms variability amplitude of 0.246. The ratio of these two quantities, at $\sim$2 (see Figure 8), indicates that red-noise variability is present (Zhang et al. 2005).

3.3. X-ray Flux Variability

The X-ray flux from Mrk 421, was monitored from 0.2 to 50 keV during this observing campaign. Many episodic outbursts are seen in all X-ray bands reported on here with the maximum emission reaching 1.7 times the mean emission level in that band for the XRT data, 2.9 times the mean emission level for that band in the ASM data, 2.7 times the mean emission level for that band in the PCA data, and 5.3 times the mean emission level for that band in the BAT data. These data are summarized in Table 3. The data are plotted in one-night bins in Figure 3 where inter-night variability in addition to overall trends are evident in the X-ray light curve. The X-ray emission in the ASM, PCA, and BAT regimes is well correlated. The night of maximum emission was MJD 53877 for the ASM data. No PCA data were taken this night and the maximum in its emission occurred on MJD 53875, which was the second brightest night for the BAT data. There is a trend toward increasing emission around this time with the previous $\sim$30 days showing elevated emission levels in the ASM, PCA, and BAT data. For the XRT light curve, which is not as well sampled as those in the other wavebands, evidence for heightened emission over a period of two nights was seen from MJD 53739 to MJD 53740. The rms variability amplitude is found to increase with energy in the X-ray regime, from 0.269 for the XRT data to 0.529 for the PCA data. As can be seen in Figure 8, the ratio of $F_{\rm var}$ to F_{pp} is found to be $\sim$2 for all X-ray data, indicative of red-noise variability.

To further study the variability properties of the X-ray light curves, the normalized, first-order structure function, $\mathrm{SF}^{(1)}(\tau)$, was computed for each light curve. $\mathrm{SF}^{(1)}(\tau)$ is defined as

$$SF^{(1)}(\tau) = \frac{1}{N} \sum \left(\frac{F(t) - F(t+\tau)}{\overline{F(t)}} \right)^2. \quad (3)$$

For a discrete time series, we calculate the structure function in bins of width $\Delta\tau$ such that the value of the structure function for a given bin is found by summing over pairs of observations separated by a time difference Δt satisfying $\tau - \Delta\tau/2 < \Delta t < \tau + \Delta\tau/2$. The structure functions for each of the X-ray bands in which substantial data were collected and for the gamma-ray data are shown in Figure 10. In all cases, the structure function is found to rise approximately linearly when plotted in log–log representation. The data from the ASM show evidence for a break between $\tau \sim 20$ and 25 days with the slope of the structure function remaining approximately constant before and after this break. The structure function of the PCA data shows evidence for a break between $\tau \sim 5$ and 8 days. Again, no significant change in the slope is seen after this break. There is clear evidence for a break in the structure function of the BAT data between $\tau \sim 55$ and 71 days after which it rises linearly once more but with a steeper slope. There are no strong features in the structure function of the gamma-ray data.

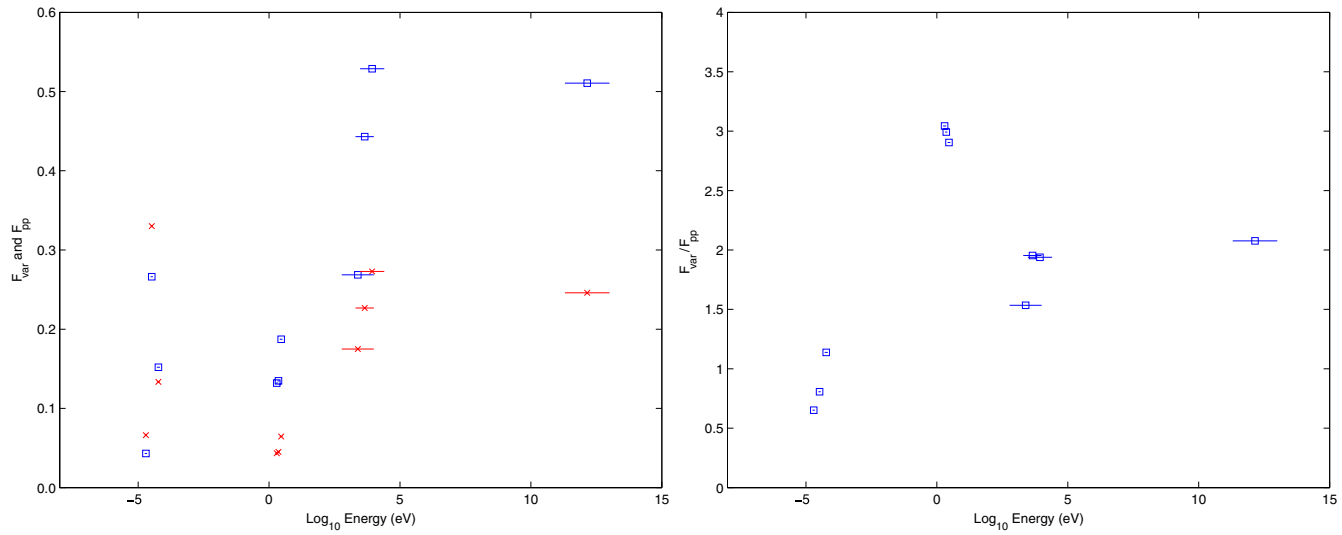

Figure 8. Left: fractional rms variability amplitude (blue squares) and the point-to-point fractional rms variability amplitude (red x's) for 10 of the 12 energy bands. Right: ratio of the fractional rms variability amplitude to the point-to-point variability amplitude as a function of energy. See the text for more details.
(A color version of this figure is available in the online journal.)

Table 3
Fractional rms Variability Amplitude, $F_{\rm var}$, and the Point-to-Point Fractional Variability Amplitude, F_{pp}, for Each of the Wavebands Explored in this Paper

Waveband	Energy Range (eV)	No. of Nights	% Nights $>3\sigma$ [a]	Mean Flux [b] (Min/Max)	$F_{\rm var}$	F_{pp}
Radio						
4.8 GHz	$1.8–2.2 \times 10^{-5}$	12	100	$6.46\ (5.8/7.5) \times 10^{-1}$	0.043	0.066
8.0 GHz	$3.0–3.6 \times 10^{-5}$	16	93.8	$5.29\ (1.5/9.9) \times 10^{-1}$	0.266	0.330
14.5 GHz	$5.2–6.8 \times 10^{-5}$	22	86.4	$4.94\ (3.3-9.0) \times 10^{-1}$	0.152	0.134
37.0 GHz	$1.5–1.6 \times 10^{-4}$	31	80.7	$3.46\ (1.4/5.3) \times 10^{-1}$	N/A	N/A
Optical						
R band	1.7–2.3	97	100	13.0 (12.6/13.3)	0.132	0.043
V band	2.1–2.5	46	100	13.4 (13.0/13.7)	0.135	0.045
B band	2.6–3.3	45	100	13.8 (13.1/14.2)	0.187	0.065
X-ray						
XRT	$0.2–10 \times 10^3$	24	100	47.2 (32.1/78.5)	0.269	0.175
ASM	$2–10 \times 10^3$	256	81.6	1.99 (−0.38/5.68)	0.443	0.227
PCA	$3–25 \times 10^3$	75	100	$5.18\ (78.3/0.14) \times 10^{-10}$	0.529	0.273
BAT	$15–50 \times 10^3$	234	42.3	$2.72\ (-6.15/14.4) \times 10^{-3}$	0.993	0.360
Gamma ray						
Whipple	$0.2–10 \times 10^{12}$	80	66.3	1.04 (−0.05/2.59)	0.511	0.246

Notes.
[a] This is the percentage of nights on which a $>3\sigma$ detection was observed.
[b] The mean, minimum, and maximum nightly averaged signal observed in each waveband during this campaign. The flux units are the same as those quoted in Figure 1.

3.4. Optical Flux Variability

The well-sampled optical light curves show evidence for variability during this campaign. The mean magnitudes for each band are shown in Table 3. When converted to linear fluxes, the optical flux was found to peak at 1.43 times its mean value in both the *R* band and the *V* band and to peak at 1.83 its mean flux in the *B* band.

Several *R*-band flare features with amplitudes of 0.2 mag are resolved in the particularly well-sampled range of dates spanning 53,800 < MJD < 53,900. The fractional rms variability amplitude and point-to-point fractional rms variability amplitude are 0.13 and 0.04, respectively, for the *R*-band light curve, 0.14 and 0.05, respectively, for the *V*-band light curve and 0.19 and 0.06, respectively, for the *B*-band light curve. In all cases, the ratio of $F_{\rm var}$ to F_{pp} is ∼3, indicating that, like the gamma-ray and X-ray bands, red-noise processes are responsible for the optical variability. The measured optical flux includes contributions from the host galaxy, estimated to be ∼15% (Nilsson et al. 1999). Since it affects only the mean flux, not the variability, the optical fractional rms variability amplitude should be about 15% higher. The level of optical variability seen in this analysis is slightly lower but is consistent with the level of variability seen in other recent MWL studies of this source (Rebillot et al. 2004).

Variations in flux among the three optical bands are highly correlated. There is weak evidence in this data set supporting a trend of flattening of the optical spectrum with increasing *R*-band flux: a trend seen more definitively by other authors in the long-term light curves of Mrk 421 and other BL Lac objects (Vagnetti & Trevese 2003; Hu et al. 2006). This behavior, predicted by several authors (Li & Kusunose 2000; Spada et al.

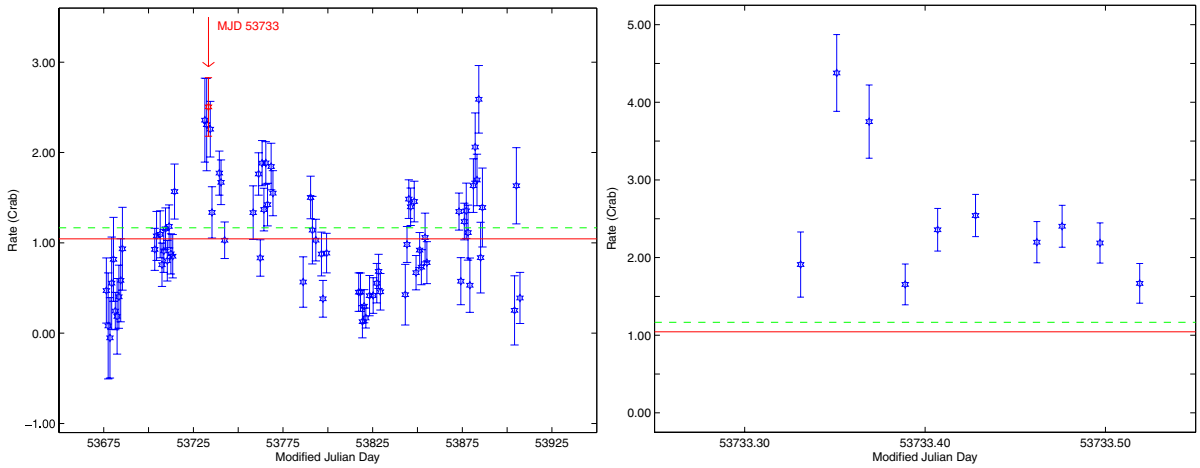

Figure 9. Left: gamma-ray light curve with the data binned in nightly bins. The mean nightly gamma-ray rate is indicated by the horizontal, solid, red line. The mean gamma-ray rate for an individual exposure (typically 28 minute) is indicated by the horizontal, dashed, green line. The night (MJD 53733) during which the maximum rate for an individual exposure was recorded is plotted in red and is also indicated by the arrow. Right: gamma-ray light curve for MJD 53733, the night during which the maximum gamma-ray rate for an individual exposure was recorded. The mean gamma-ray rate recorded during the entire campaign for an individual exposure is indicated by the horizontal, dashed, green line. Note that a different scale is used on the *Y*-axis in each figure.

(A color version of this figure is available in the online journal.)

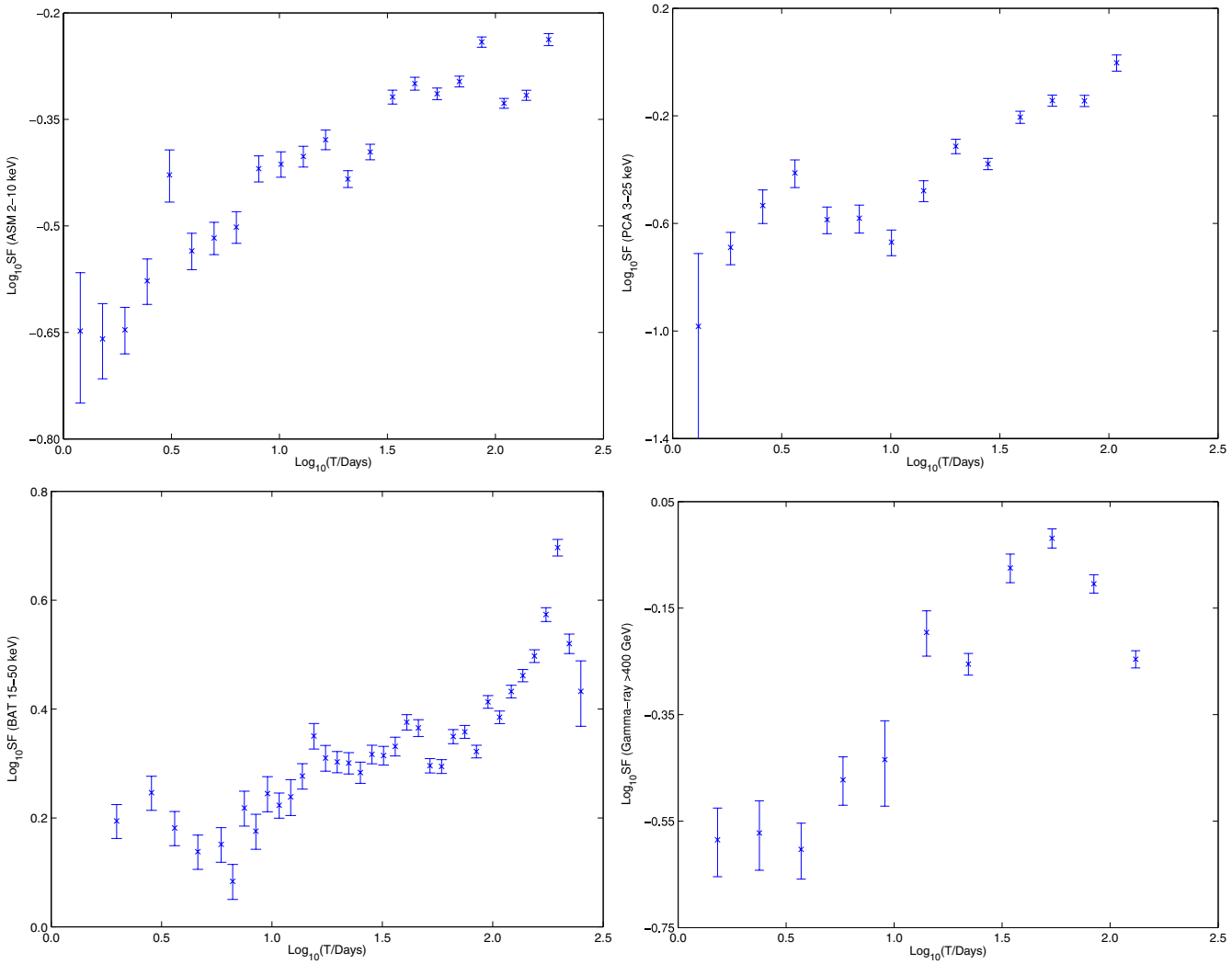

Figure 10. Normalized, first-order structure function for the ASM data (top left), the PCA data (top right), the BAT data (bottom left), and the gamma-ray data (bottom right).

(A color version of this figure is available in the online journal.)

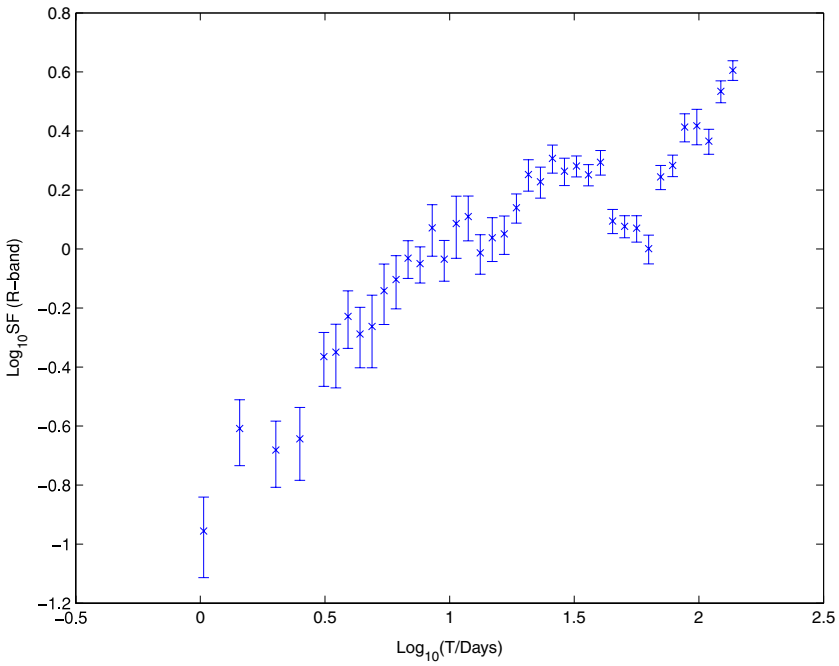

Figure 11. Structure function for the *R*-band optical data.
(A color version of this figure is available in the online journal.)

2001; Vagnetti et al. 2003), is consistent with the expected spectral variability behavior of a jet with emission dominated by the SSC processes.

The normalized, first-order structure function of the composite *R*-band light curve has been computed and is shown in Figure 11. The structure function rises approximately linearly at short timescales up to a time lag of between about 40 and 60 days where a clear break is seen, above which the structure function rises linearly again. The break most likely indicates a characteristic timescale of shotlike emission events. We note that structure functions with similarly shaped breaks have been observed in other wavebands with different characteristic break frequencies, for example, the EUV emission from Mrk 421 recorded by the *Extreme Ultraviolet Explorer* during a 1998 MWL campaign (Takahashi et al. 2000).

3.5. Radio Flux Variability

This is the waveband in which the light curves are least sampled and also, the waveband in which the least amount of variability is seen. This is typical for blazars; the variations observed in the radio regime tend to occur over longer timescales than those at shorter wavelengths (Kovalev et al. 2002; Błażejowski et al. 2005; Rebillot et al. 2006; Hovatta et al. 2007). This is supported by the fact that the lowest values of the fractional rms variability amplitude, 0.04–0.27, were found for the radio data. The fact that these data were less well sampled than the data at other frequencies would most likely lead to an underestimation of $F_{\rm var}$ in this waveband. The ratio of $F_{\rm var}$ to F_{pp} for each of the four radio bands plotted in Figure 8 is found to be $\sim$1, indicative of white-noise variability.

3.6. X-Ray Correlations With Gamma-Ray Data

All of the X-ray data taken during this campaign are plotted with the gamma-ray data in Figure 3. For this plot, the XRT and PCA data are plotted between 2 and 10 keV, their counts having been converted to fluxes using a log-parabolic model to fit the data. The length of the exposure acquired varies from night to night, even for a single instrument. There is evidence for correlated variability throughout the campaign, in particular, around the period of MJD 53875 to MJD 53885. The mean rate over the entire observing campaign for each waveband is plotted as a horizontal, solid red line on these plots. The data can be seen to follow similar trend in terms of their mean flux level. Figure 12 shows flux–flux diagrams (for 1-day timescales) for each X-ray band with the gamma-ray data. Each data set was first normalized by dividing each flux point by the mean flux in that waveband so that the flux–flux correlations between the gamma-ray data and each X-ray band could be more easily compared. Using a weighted total least-squares algorithm (Anton 2007), which took into account uncertainties in the X-ray and the gamma-ray data, a straight line was fitted to each of the flux–flux plots. The slopes of these lines are found to increase with X-ray energy and are 0.73, 1.00, 1.51, and 3.01 for the XRT, ASM, PCA, and BAT data, respectively. As would be expected due to their overlap in energy range, the slopes of the flux–flux relations between the gamma-ray and the XRT (0.2–10 keV), ASM (2–10 keV), and PCA (3–25 keV) data are quite close to each other, their differences presumably arising due to the slightly different energy ranges and measurement uncertainties. Although the lower energy X-ray data (i.e., not those from the BAT) and gamma-ray data do look somewhat correlated, there are outliers on all plots. In general, the gamma-ray and the lower energy X-ray data exhibit low and high fluxes at similar times. To compare the relationship between these X-ray and gamma-ray data with that derived by Fossati et al. (2008), the data were replotted on a log scale, with the gamma-ray data on the *Y*-axis (Figure 13). The slopes of the lines were found to be 1.03 for the XRT (0.2–10 keV), 0.98 for the ASM (2–10 keV), 0.48 for the PCA (3–25 keV), and 0.22 for the BAT (15–50 keV) data. In the energy range between 2 and 10 keV, Fossati et al. (2008) found a slope of 0.88, similar to that found here in that energy range, for the relationship between the PCA and gamma-

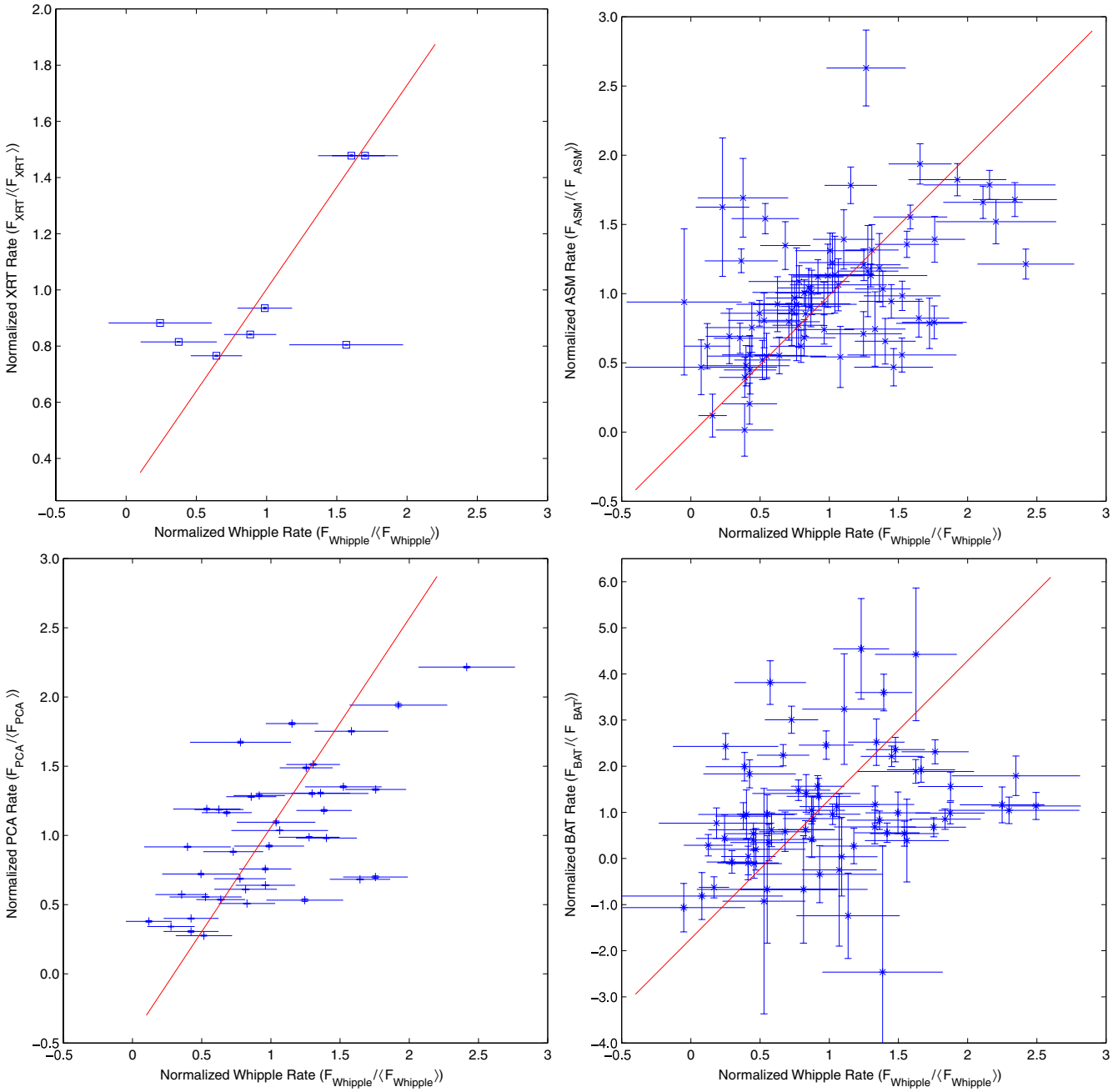

Figure 12. Flux–flux correlation for top left: the gamma-ray and XRT data (slope 0.73); top right: the gamma-ray and ASM data (slope 1.00); bottom left: the gamma-ray and PCA data (slope 1.51); bottom right: the gamma-ray and BAT data (slope 3.01). Note that for the ASM and PCA data the scales on the *x*- and *y*-axes are equal, while for the XRT data, the scale on the *x*-axis is twice that of the *y*-axis, while for the BAT data, the scale on the *y*-axis is three times that of the *x*-axis.

(A color version of this figure is available in the online journal.)

ray data from Mrk 421. When only the significant detections (defined here as $>3\sigma$ and highlighted in green in Figure 13) were included in the slope calculation, the higher flux data remained and the slopes of the XRT, ASM, and PCA data decreased slightly to 0.94, 0.78, and 0.33, respectively, while the relationship between the BAT and the gamma-ray data became inverted (slope of -0.18), with little evidence for correlation between the two bands. Flux–flux diagrams were also made for weekly and monthly timescales. The ASM data, in particular, were found to show evidence for correlated emission with the gamma-ray data on weekly and on monthly timescales as shown in Figure 14. The slopes of the lines are 1.0, 1.0, and 0.5 for the daily, weekly, and monthly light curves, respectively.

Figure 15 shows the flux divided by the mean flux in that band for each of the X-ray data sets and for the gamma-ray data. A high degree of correlation can be seen, in particular, between the gamma-ray data and those from the ASM and the PCA.

We searched for correlations between fluxes in the X-ray bands and the gamma-ray band using the DCF. The DCF, introduced by Edelson & Krolik (1988), is an approximation to the classical correlation function which is applicable to discrete time series. It gives the linear correlation coefficient (R) for two light curves as a function of the time lag between them. The DCF is well suited to sparsely sampled light curves and is less likely to give rise to spurious results than a traditional correlation

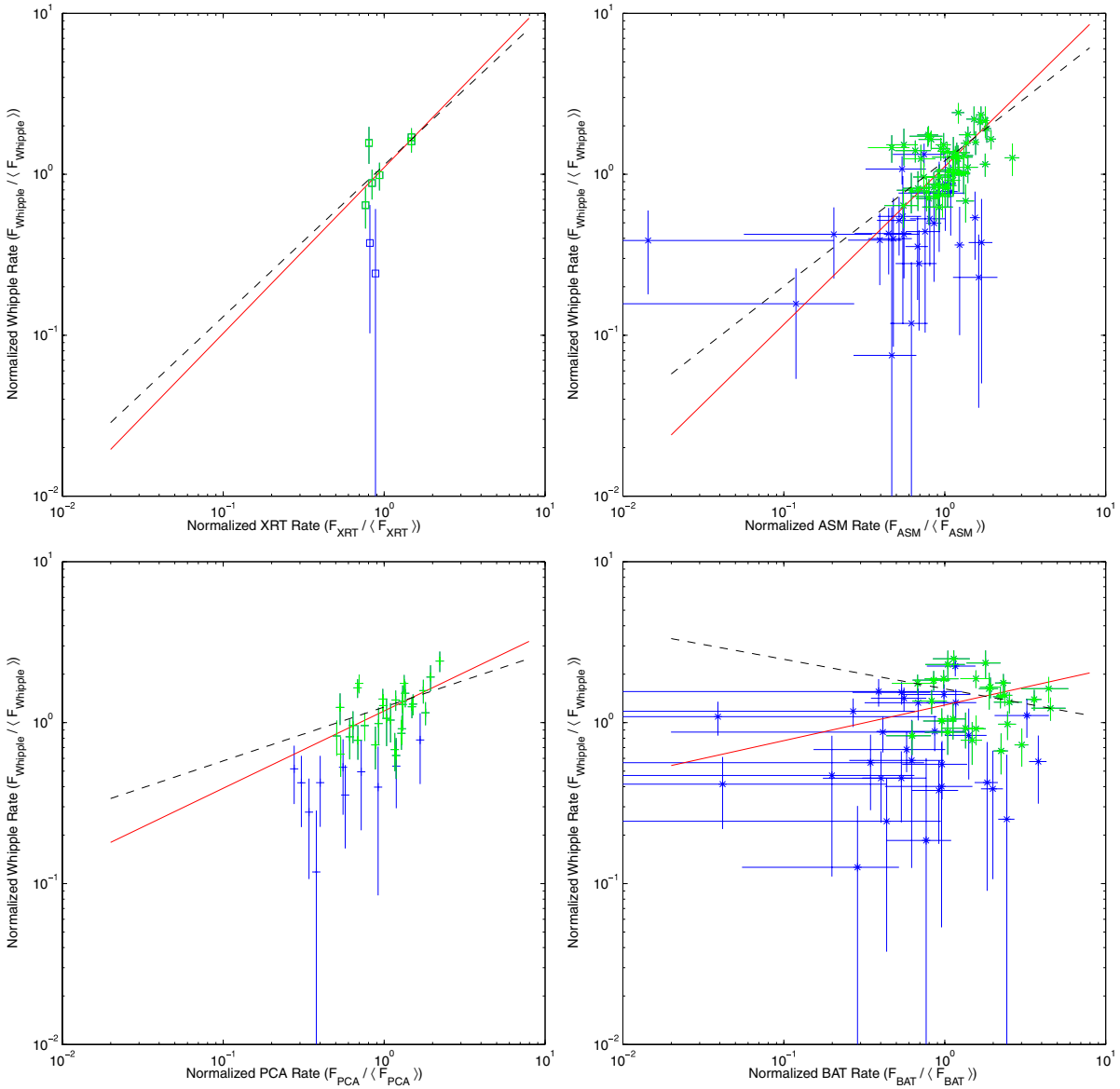

Figure 13. Flux–flux correlation on a log scale for the X-ray and gamma-ray data. The solid, red lines show the slope when all the data are included, while the black, dashed lines show the slope when only the data with significance $>3\sigma$ (highlighted here in green) are included. Top left: the gamma-ray and XRT data—slopes 1.03 (all), 0.94 ($>3\sigma$); top right: the gamma-ray and ASM data—slopes 0.98 (all), 0.78 ($>3\sigma$); bottom left: the gamma-ray and PCA data—slopes 0.48 (all), 0.33 ($>3\sigma$); bottom right: the gamma-ray and BAT data—slopes 0.22 (all), -0.18 ($>3\sigma$).

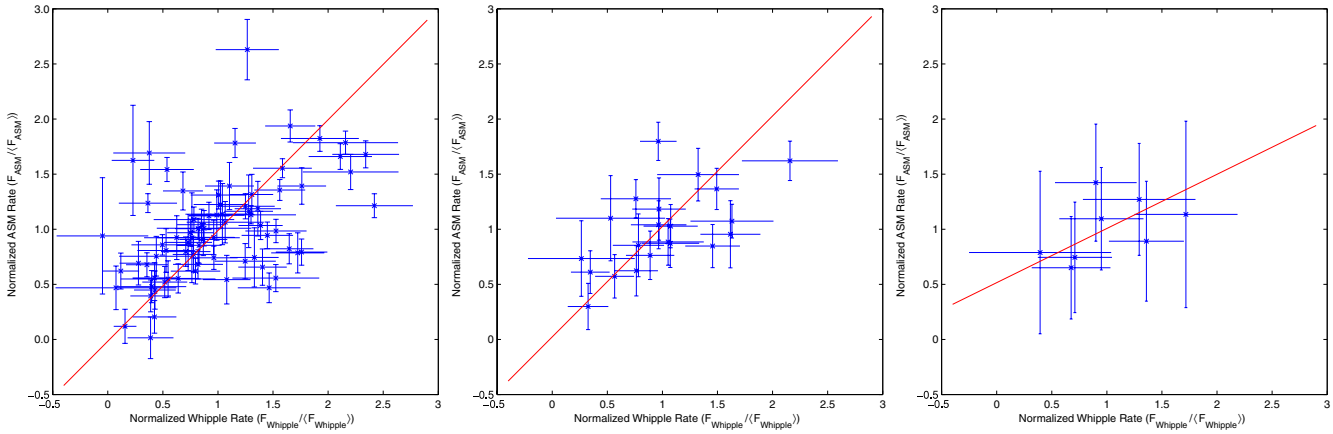

Figure 14. Flux–flux correlation for the gamma-ray and ASM data on different timescales. Left: the daily binned gamma-ray and ASM data (slope 1.00); middle: the weekly binned gamma-ray and ASM data (slope 1.00); right: the monthly binned gamma-ray and ASM data (slope 0.49).

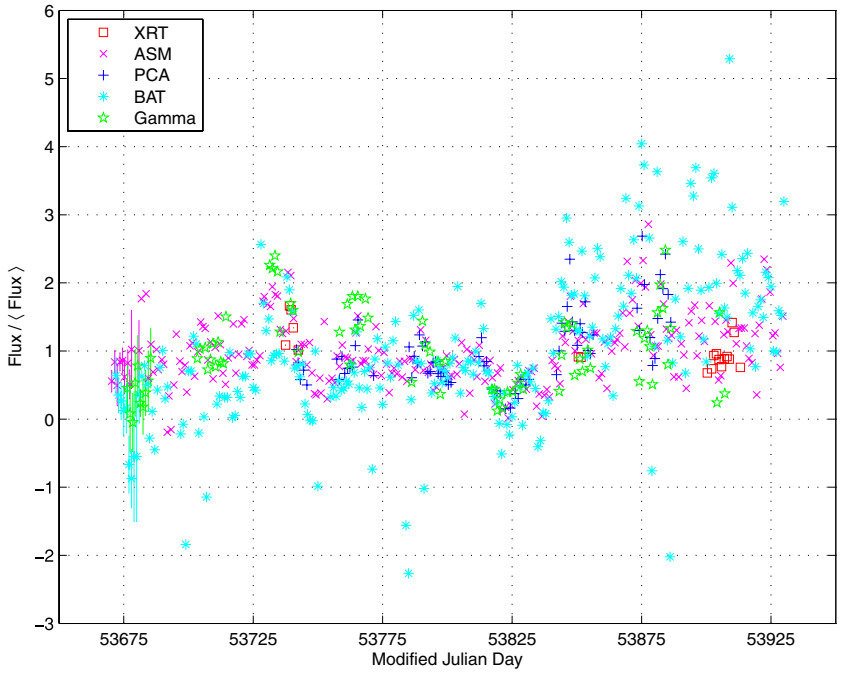

Figure 15. For each of the four X-ray data sets and for the gamma-ray data, the flux is plotted over the mean flux in that band. For each data set, the error bars are plotted for the first 10 data points so that the typical magnitude of the uncertainties for each waveband are conveyed.
(A color version of this figure is available in the online journal.)

analysis with interpolated light curves. To construct the DCF, we first collect the set of unbinned discrete correlations, UDCF_{ij},

$$\mathrm{UDCF}_{ij} = \frac{(a_i - \overline{a})(b_j - \overline{b})}{\sqrt{(\sigma_a^2 - e_a^2)(\sigma_b^2 - e_b^2)}} \quad (4)$$

for all pairs of observations a_i, b_j, with measurement errors σ_a, σ_b, and mean measurement errors of e_a, e_b, respectively. Each pair is associated with a time lag $\Delta t_{ij} = t_j - t_i$. The DCF for a given time lag, τ, is then constructed as

$$\mathrm{DCF}(\tau) = \frac{1}{M} \sum \mathrm{UDCF}_{ij}, \quad (5)$$

where the sum runs over the M pairs of observations separated by $\tau - \delta t/2 < \Delta t_{ij} < \tau + \delta t/2$, where δt is the chosen bin width. The uncertainty on the value of the DCF in a given bin is calculated as the rms variance of all the contributing UCDF_{ij} about the value $\mathrm{DCF}(\tau)$.

The DCF for each of the X-ray bands with the gamma-ray data is shown in Figure 16. In these plots, the x-axis is defined such that in the gamma–PCA DCF for example, a positive lag means that the gamma-ray data lagged the X-ray data. For the XRT–gamma-ray DCF, 4-day binning is used due to the sparsity of the XRT data. For the ASM–gamma-ray DCF, 1-day binning is used and, for the PCA- and BAT–gamma-ray DCF, 2-day binning is used. According to both the SSC and EC models for blazar emission, the same population of electrons is responsible for the X-ray and the gamma-ray emission. Therefore, the X-ray and gamma-ray light curves should be correlated. For the well sampled ASM, PCA, and BAT light curves, a zero-lag correlation is seen clearly, with peak values of the DCF at zero lag of 0.44, 0.56, and 0.39, respectively. The shape of the DCF looks similar for the BAT and ASM data, as their light curves are similar. The PCA data have the smallest uncertainties and also show the highest DCF value at zero lag.

To measure the chance probability of accidental correlations in the DCF, the Monte Carlo method described in Jordan (2004) was employed. Taking a correlation at zero lag as the a priori hypothesis, the chance probability of obtaining the measured value of the DCF at zero lag, with the assumption that the times of the flares are randomly sequenced, was calculated. 100,000 light curves were simulated with the same characteristic timescale as the PCA, determined by the SF analysis (Section 3.3). The DCF was calculated for each of these simulated light curves and the gamma-ray light curve. The chance probability of obtaining a DCF value at or above 0.56 from this Monte Carlo method was found to be 0.1%. We can state, therefore, with reasonable confidence that the gamma-ray and PCA X-ray data are correlated within 1.5 days.

3.7. Optical Correlations With Other Wavelengths

Figure 17 shows the flux–flux correlation for the gamma-ray and optical data (linear fluxes). Each data set was first normalized by dividing each flux point by the mean flux in that waveband so that the flux–flux correlations between the gamma-ray and optical data could be more easily compared. Using a weighted total least-squares algorithm (Anton 2007), which took into account uncertainties in the optical and the gamma-ray data, a straight line was fitted to each of the flux–flux plots. Although not well correlated, the data do show a somewhat negative correlative trend, with the high-flux gamma-ray points tending to coincide with the low-flux optical points and vice versa. The slopes of the lines shown in Figure 17 are found to decrease marginally as energy increases, with a slope of -0.60 in the R band, -0.43 in the V band, and -0.40 in the B band.

We searched for correlations between fluxes in the optical R band, which was the best sampled of the optical light curves, and all other nonoptical wavebands presented in this investigation using the DCF. Of all the pairs of wavebands investigated, only

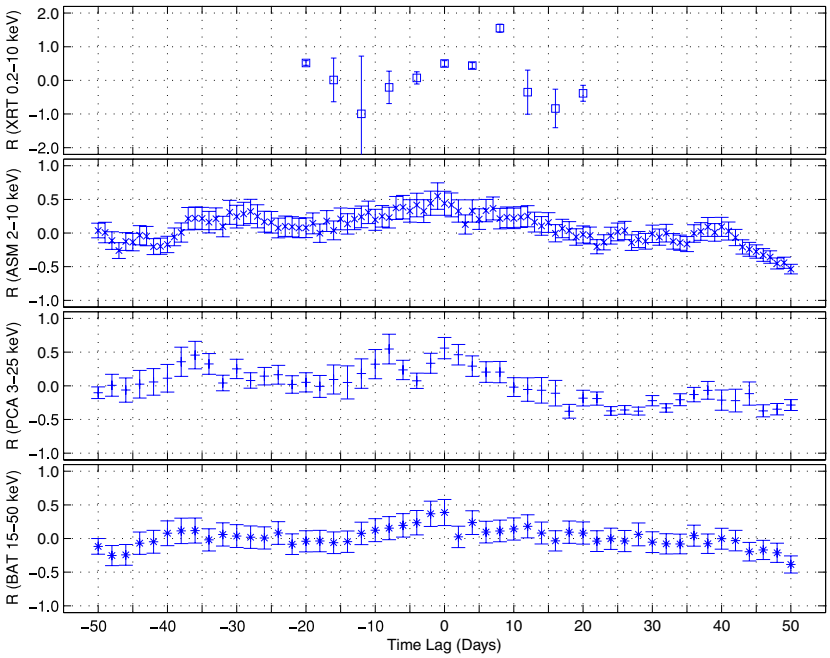

Figure 16. DCFs between top: the TeV and XRT light curves with 4-day bins due to the sparsity of the XRT data points; second from top: the TeV and ASM light curves with 1-day bins; second from bottom: the TeV and PCA light curves with 2-day bins; bottom: the TeV and BAT light curves with 2-day bins; the *x*-axes are defined such that a positive value of *R* means that the X-rays precede the gamma rays.

(A color version of this figure is available in the online journal.)

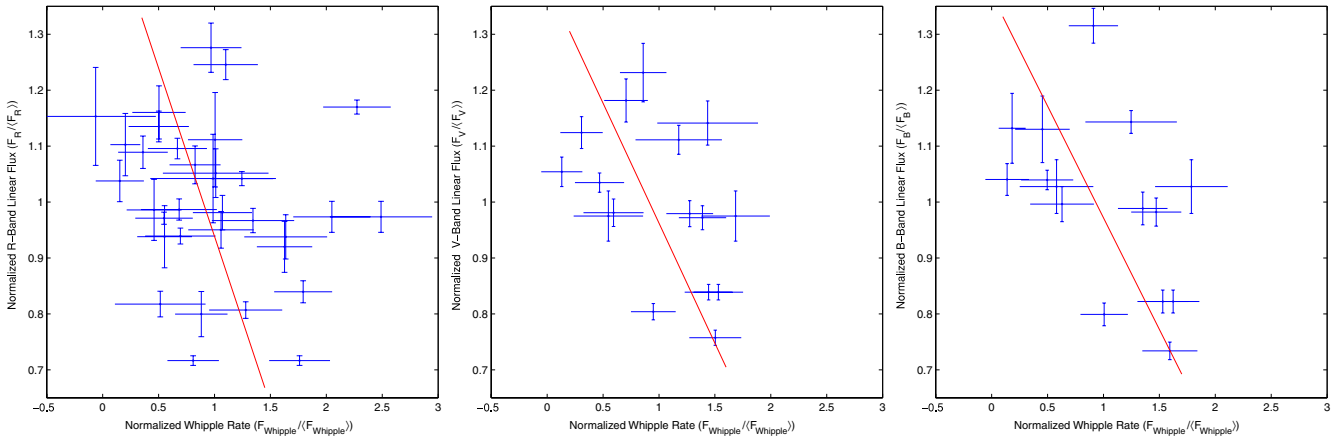

Figure 17. Flux–flux correlation for left: gamma-ray and *R*-band optical data (slope −0.60); middle: gamma-ray and *V*-band optical data (slope −0.43); right: gamma-ray and *B*-band optical data (slope −0.40). Note that the range of the gamma-ray data is five times that of the optical data.

(A color version of this figure is available in the online journal.)

the DCF between the optical and TeV light curves, presented in Figure 18, shows noteworthy features. The DCF indicates a possible optical-TeV correlation with the optical flux lagging the TeV flux by about 7 days. An elevated level of correlation is also seen with the optical leading the TeV by 25 to 45 days (Steele et al. 2008).

We investigated the significance of these possible correlations using simulated optical light curves with the same variability properties as the observed *R*-band light curve. The simulated optical light curves were generated deterministically as a superposition of harmonic oscillators with random phases whose frequencies are integer multiples of a fundamental frequency corresponding to the total length of the campaign. The amplitude of an oscillator at a given frequency is drawn from a power spectral density (PSD) function derived from the first-order structure function of the observed *R*-band light curve. Assuming the process(es) responsible for the optical variability are stationary over the period of observation, the slope of the PSD, β, at a given frequency is related to the slope of the first-order structure function, α, by $\beta = 1 + \alpha$. Using this relation, we derive the PSD of our simulated light curves by a fit to the first-order structure function that rises linearly with a slope $\alpha = 0.568$ until the beginning of the break at $t = 39.8$ days, is flat ($\alpha = 0$) between 39.8 days $< t <$ 63.0 days, and then rises again with slope $\alpha = 1.700$.

After multiple realizations of the campaign using simulated optical light curves which are, by definition, not correlated with the TeV light curve, we can assess the probability to have seen the observed correlation features due to chance. For each realization, we compute the DCF between the simulated optical

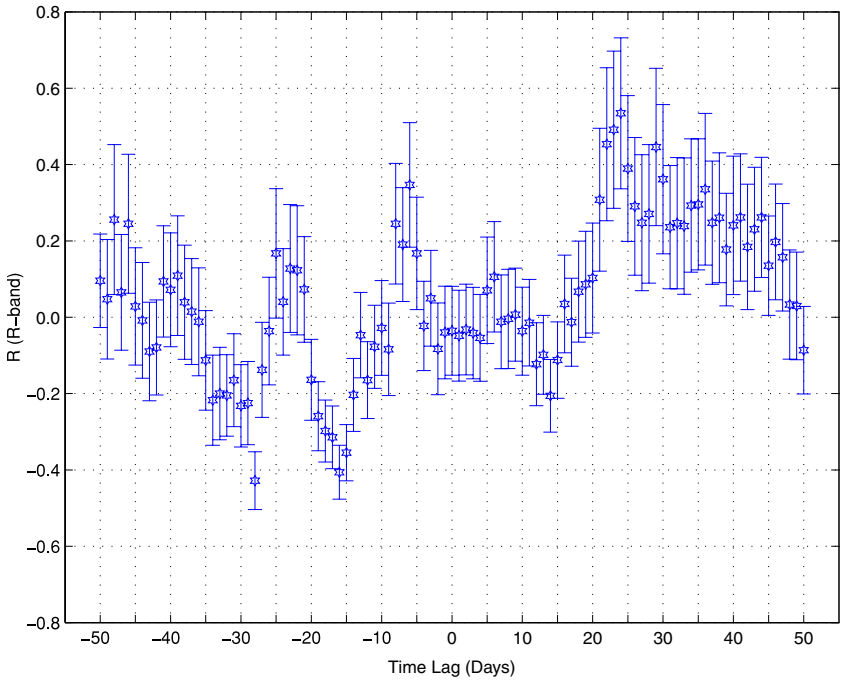

Figure 18. DCF of the optical *R*-band and gamma-ray data. The *x*-axis is defined such that a positive value of *R* means that the optical photons precede the gamma rays.

(A color version of this figure is available in the online journal.)

and the real TeV light curves. For each bin of the DCF, we record the values of the correlation coefficient, R, its error, σ_R, and the test statistic $S = R/\sigma_R$. After many realizations, we build the distribution of S seen in each bin of the DCF and compute the chance probability to have found the observed value of $S = S_{\rm obs}$ or higher by integrating the distribution above $S_{\rm obs}$. This gives us the chance probability of having observed a given correlation in a particular bin, but it does not speak to the likelihood of correlation *features* involving more than one bin. To assess the likelihood of the observed DCF features as a whole, we construct two more distributions, $\mathcal{L}_{\pm} = \prod_i p_i$ where for $\mathcal{L}_-$ the product runs over all DCF bins, i, with $\tau < 0$, and for $\mathcal{L}_+$ the product runs over bins with $\tau \geqslant 0$. Using these two distributions, we find the likelihood to have observed the optical precursor (postcursor) features by chance to be 20% (60%). Further investigation reveals that the DCF feature seen at $\tau = 7$ days probably arises due to contamination from the *R*-band autocorrelation function, which also exhibits features at multiples of 7 days. The possible reality of the optical precursor emission is more difficult to assess since our method assesses all the correlation features on a given side of the DCF at once. Unfortunately, it would not have been possible to narrow the likelihood computation to smaller range of τ in order to assess a particular feature without subjecting the result to an unknown trials penalty.

3.8. Spectral Energy Distribution

SEDs are shown on three representative dates in Figure 19 when the VHE emission was at a high (MJD 53763; filled blue squares), medium (MJD 53852; open green circles), and low (MJD 53820; closed red triangles) emission level; these dates were chosen because there were MWL data available over the full spectrum. They were not chosen where there was the best correlation with the flux at X-ray wavelengths and hence the SEDs are more typical. These nights are marked on the gamma-ray light curve in Figure 2. On MJD 53763, 135 minutes of noncontiguous gamma-ray data were taken; on MJD 53852, 138 minutes of noncontiguous gamma-ray data were taken, while on MJD 53820, 90 minutes of noncontiguous gamma-ray data were taken. The optical data shown on the SED has the galaxy contribution subtracted. There was no significant variation in the radio fluxes over the three dates. The X-ray spectrum for the PCA data was obtained using XSPEC,[39] while the TeV spectrum was obtained using the forward-folding method described in Rebillot et al. (2006). Mrk 421 was in the field of view of the BAT during parts of each of the three observations. It was detected on MJDs 53763 and 53852 and upper limits were obtained for MJD 53820. A spectral analysis of the BAT survey mode data on Mrk 421 was performed for two nights, MJDs 53763 and 53852. The BAT data from these nights comprised 74 and 44 minutes, respectively, and were processed using standard *Swift* FTOOLS[40] to remove the diffuse background and the effects of other bright point sources in the field of view. Eight-channel spectral and response files were produced for the position of Mrk 421 for each observation and were fit using XSPEC 11 to a simple power-law model to provide fluxes in the energy range of 14–195 keV. The highest energy at which a significant detection was made with the BAT was 75 keV.

The data from the nights chosen to represent the high-state and medium-state of Mrk 421 are plotted in Figures 20 and 21 along with archival Mrk 421 data (Buckley 2000). The dashed purple lines show the synchrotron and self-Compton distributions for the parameters given in Table 4. The black dot-dashed curves show a hypothetical black-body component peaked at 1 μm and the corresponding EC component. The red solid line shows the sum of the SSC and EC models fitting results, which, in both cases, is in good agreement with the simultaneous optical, X-ray, and gamma-ray data.

[39] http://heasarc.nasa.gov/xanadu/xspec/
[40] http://heasarc.gsfc.nasa.gov/docs/software/lheasoft

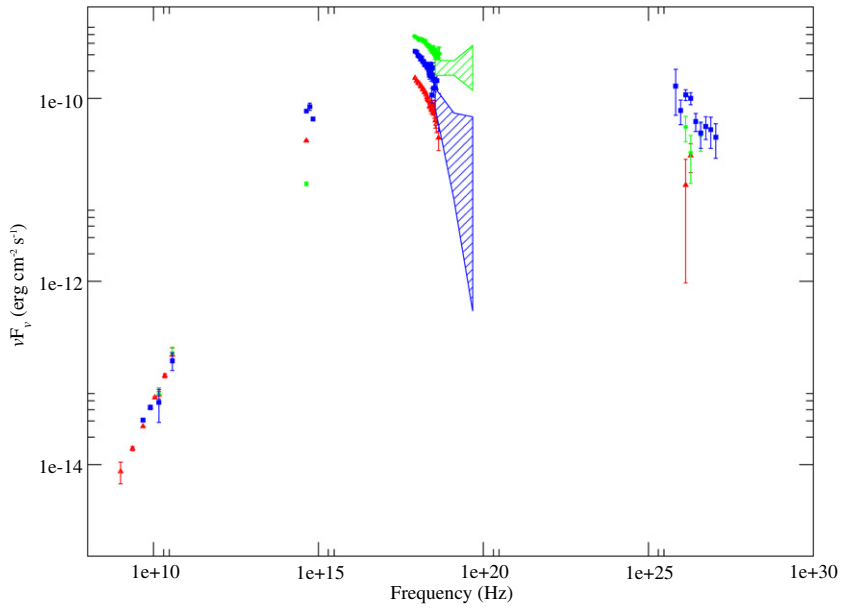

Figure 19. SED for Mrk 421 on three nights during this MWL campaign when the VHE emission, as defined by the gamma-ray data, was at high (MJD 53763; filled blue squares), medium (MJD 53852; green filled circles), and low (MJD 53820; closed red triangles) emission levels.

(A color version of this figure is available in the online journal.)

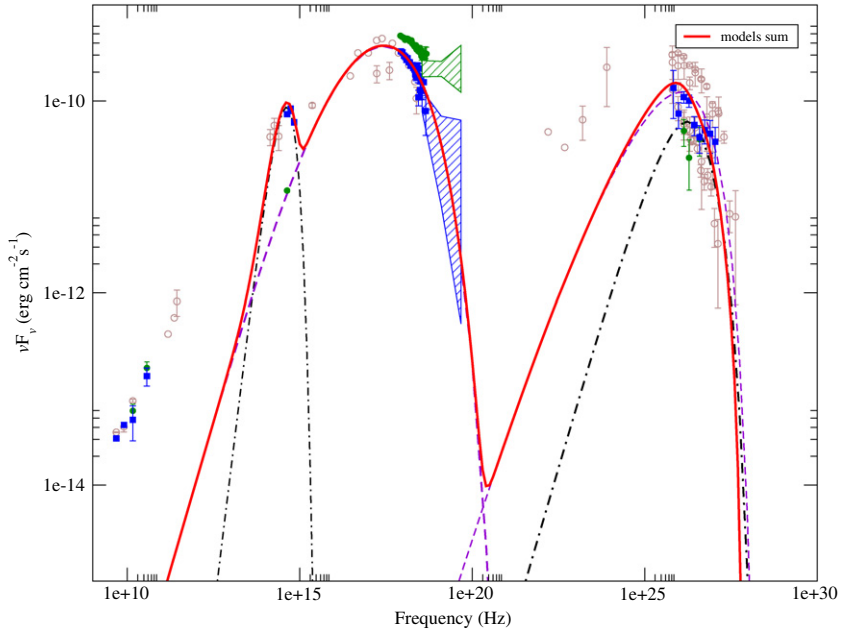

Figure 20. Fit of simple model to the SED for Mrk 421 on MJD 53763, the high-state night data (as defined by the gamma-ray data) are shown for all wavebands as blue filled squares. For reference, the data from the medium-state night (Figure 21) are also shown (green filled circles). Archival data are shown as brown open circles (Buckley 2000). Details of the model fit to the data are given in the text. The data are fit with a combined SSC and EC model. The dashed purple line shows the synchrotron and self-Compton distributions for the parameters given in the text. The black dot-dashed curve shows a hypothetical black-body component peaked at 1 μm and the corresponding EC component. The red solid line shows the sum of the SSC and EC models fitting results, which is in good agreement with the simultaneous optical, X-ray, and gamma-ray data. The archival data on the SED show that the level of the radio emission did not change significantly over the past 10 years. The 2005–2006 radio data were taken within +6/−5 days of the low-, medium-, and high-state data.

(A color version of this figure is available in the online journal.)

4. DISCUSSION AND CONCLUSION

The Mrk 421 observations presented in this paper comprise one of the most comprehensive data sets, both in terms of spectral and temporal coverage, ever accumulated on a blazar. The well-sampled optical light curves, in particular, differentiate this campaign from others undertaken previously. Like some of these, this campaign was not triggered by Mrk 421 entering some predefined emission state. Rather, data were gathered regardless of the flux level observed from Mrk 421 in any particular waveband. Great care was taken to ensure that the data were calibrated properly in each waveband so that the effects of changing atmospheric conditions, nightly sky-brightness fluctuations or instrumental differences were removed from the data.

The broadband temporal variability of Mrk 421 was examined by computing the fractional rms variability amplitude and the point-to-point fractional rms variability amplitude for each

Table 4
The Model Parameters Used for Fitting the Broadband SED of Mrk 421, Shown in Figures 20 and 21

Parameter	Value
Doppler factor	90
Magnetic field in the bulk frame	0.12 G
Electron energy density compared with equipartition value	0.3
Electron spectral index	1.5
Size of emission region	$70R_{\rm Sch}$
Electron mean free path compared with gyroradius (Bohm limit)	20
Cooling time at maximum electron energy	2.25 minutes
Acceleration time at maximum electron energy	2.25 minutes
Shock velocity in bulk frame	$0.02c$
Soft photon peak wavelength	1.0 μm
Mass of black hole	$10^8\ M_\odot$

waveband in which it was detected consistently throughout the campaign. A general trend of increasing $F_{\rm var}$ toward higher frequencies was observed, with the radio and optical data exhibiting very low variabilities while the X-ray and gamma-ray data had high fractional rms variability amplitudes. Błażejowski et al. (2005) probed the fractional rms variability amplitude for Mrk 421 data taken during 2003–2004. These data covered a subset of the wavebands presented here (14.5 GHz radio, *R*-band optical, 3–25 keV X-ray, and 0.2–20 TeV gamma ray) and, like the 2005–2006 data, were binned in 1-day bins. Except for the 14.5 GHz radio data, $F_{\rm var}$ was always larger for the 2003–2004 data set. In general, however, the differences between the $F_{\rm var}$ values for the 2005–2006 data and 2003–2004 data, are small, ranging between 15% and 33%.

Fossati et al. (2000) measured $F_{\rm var}$ for Mrk 421 in 1997 and 1998 in the X-ray range from 0.26 to 4.76 keV using data taken with *BeppoSAX*. A trend of increasing $F_{\rm var}$ with increasing energy was observed. The fractional rms variability amplitudes computed here for the X-ray data during 2005–2006 were all higher than those obtained in 1997–1998. However, the 1997–1998 data had much finer binning applied (200–2500 s) and covered a narrower energy range (0.26–4.76 keV) than the light curves shown here so, although the same trend of increasing $F_{\rm var}$ with energy was observed, the variability was being probed on different timescales and over a different energy range than those shown here. Giebels et al. (2007) found evidence for a power-law behavior of $F_{\rm var}$ over four decades of energy for Mrk 421 on MJD 51991 to MJD 51992, with $F_{\rm var} \propto E^{0.24\pm0.01}$. Figure 22 shows $F_{\rm var}$ as a function of energy for Mrk 421 during the campaign presented here. The uncertainties on $F_{\rm var}$ were calculated as described in Vaughan et al. (2003). Unlike the data from MJDs 51991 and 51992, the 2005–2006 data are not well described by a power-law fit. The timescales being probed are much longer here however, and also, a larger energy span (15 decades) is available so the engine is being probed in quite a different regime.

The BAT data (15–50 keV) had the highest value of $F_{\rm var}$ at 0.993 but, due to the fact that a statistically significant detection (defined here as $>3\sigma$) was only obtained on 42.3% of the nights, the BAT data are not considered a consistently significant enough detection to include their $F_{\rm var}$ and F_{pp} values in the final analysis. The BAT energy band falls just at the upper end of the synchrotron peak for Mrk 421 so, presumably, given that the synchrotron peaks of BL Lac objects are known to shift in strength and in energy on many timescales, there were many nights on which the X-ray flux from Mrk 421 was below the detection threshold of the BAT due to the shifting synchrotron peak. X-ray photons were detected up to 75 keV with the BAT during this campaign with no significant detection above these energies. The BAT energy regime was the waveband in which the most dramatic increase (a factor of 5.3) over the mean flux level, which was usually very low, was observed. This occurred on MJD 53909, after the end of the gamma-ray observing campaign. The second and third highest nights in the BAT energy regime were MJDs 53875 and 53876, when fluxes of 4.0 and 3.7 the mean level (respectively) were observed. No gamma-ray data were taken on MJD 53875 but on MJDs 53874 and 53876, the gamma-ray flux was at 0.55 and 1.30 its mean level. The maximum nightly gamma-ray rate of 2.5 times the mean nightly rate was recorded approximately 10 days later on MJD 53884. As can be seen in Figure 15, the X-ray and gamma-ray data are, in general, correlated with similar levels of fluctuation being present in the lower energy X-ray data (XRT, ASM, and PCA) and the gamma-ray data but with larger variations often occurring at the higher energies covered by the BAT.

As shown in Figures 12 and 13, where all data taken within one day of each other are plotted, there is evidence for a correlation between the gamma-ray data and the XRT, ASM, and PCA data (i.e., 0.2–25 keV) in both linear and log-space but, no evidence for a positive correlation with the BAT data (15–50 keV). The slopes of the best-fit lines to the X-ray and gamma-ray data in Figure 13 are consistent with that found by Fossati et al. (2008) in the 2–10 keV band when, unlike during the campaign described here, Mrk 421 was in an active state.

Figure 14 shows the flux–flux correlation for the gamma-ray and ASM data on daily, weekly, and monthly timescales. The data show evidence for correlation on all of these timescales. The DCF shows a similar shape for the ASM, PCA, and BAT data with a peak visible at zero-lag for each data set (Figure 16). As described in Section 3.6, simulated light curves indicated that the chance probability of this feature for the PCA data is low (0.1%), lending support to SSC and EC models, where the X-ray and gamma-ray emission are produced by the same population of accelerated electrons.

The well-sampled optical light curve, in particular that in the *R* band, allowed a detailed correlation analysis to be carried out between the optical and TeV data. As can be seen in Figure 17, these data were not found to be well correlated. Although a peak at -7 days was seen in the optical–gamma-ray DCF (Figure 18), indicating that the optical lags the TeV, it was shown that the likelihood of seeing such a peak by chance was 20% and that a feature in the autocorrelation function of the *R*-band data, which occurs at multiples of 7 days, was likely responsible for this feature in the DCF.

For the high- and medium-state nights (MJDs 53,763 and 53,852, respectively), we compare our results to a simple one-zone SSC model with an EC component. We make an ad hoc assumption of Comptonization of a one micron emission component reflected back into the jet. Using the prescription of Inoue & Takahara (1996), we determine the break energy and maximum energy of the electron spectrum using a simple model of diffusive shock acceleration. While the fraction of light scattered back into the jet is a completely free parameter, the maximum electron energy, pair absorption in the source, and shape of the IC peak are all determined in a self-consistent way. The resulting model fits to the SED are shown for the high-state night in Figure 20 and for the low-state night in Figure 21. We note that the light curves of Mrk 421 in this campaign as

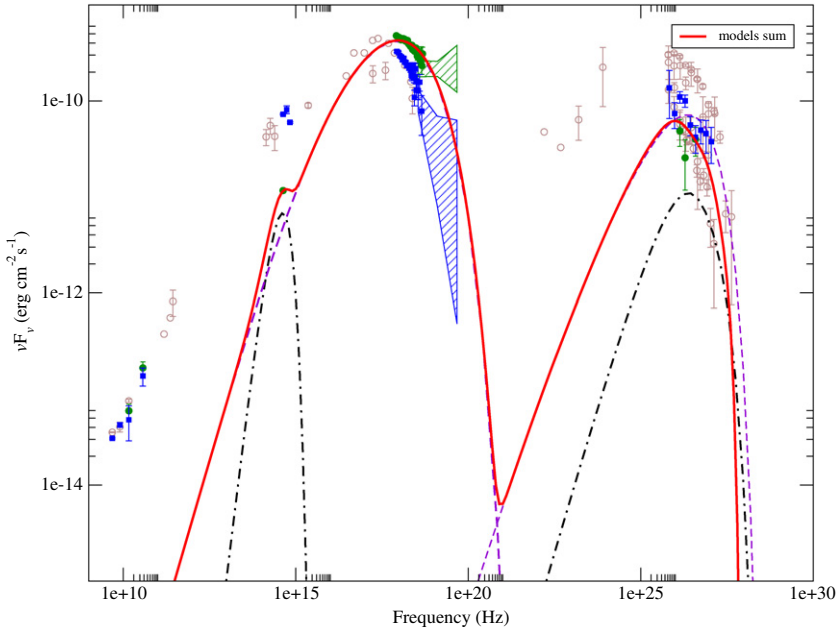

Figure 21. Fit of simple model to the SED for Mrk 421 on MJD 53852, the medium-state night data (as defined by the gamma-ray data) are shown for all wavebands as green filled circles. For reference, the data from the high-state night (Figure 20) are also shown (blue filled squares). Archival data are shown as brown open circles (Buckley 2000). Details of the model fit to the data are given in the text. The data are fit with a combined SSC and EC model. The dashed purple line shows the synchrotron and self-Compton distributions for the parameters given in the text. The black dot-dashed curve shows a hypothetical black-body component peaked at 1 μm and the corresponding EC component. The red solid line shows the sum of the SSC and EC models fitting results, which is in good agreement with the simultaneous optical, X-ray and gamma-ray data. The archival data on the SED show that the level of the radio emission did not change significantly over the past 10 years. The 2005–2006 radio data were taken within +6/−5 days of the low-, medium-, and high-state data.

(A color version of this figure is available in the online journal.)

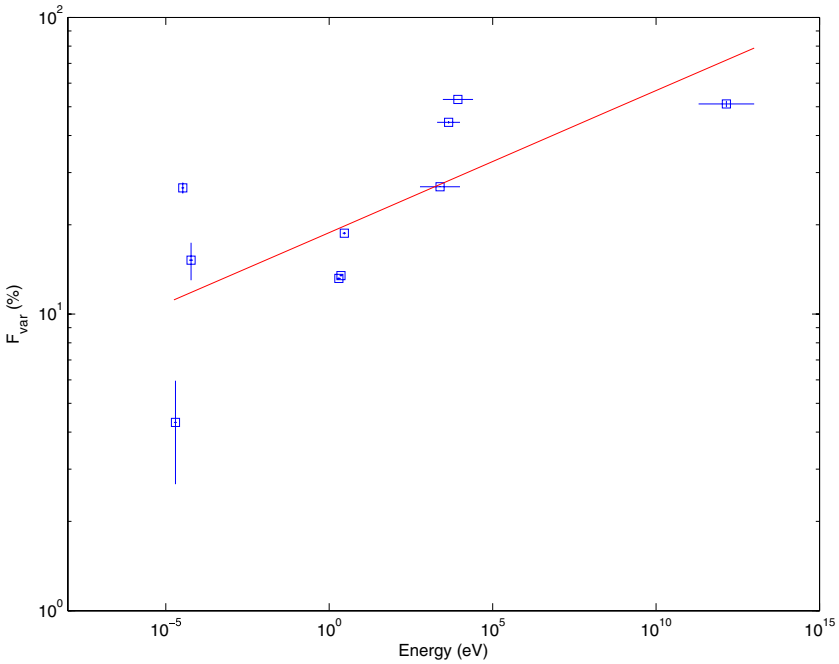

Figure 22. Fractional rms variability amplitude as a function of energy. The red line shows the best-fit power law to these data. Unlike previous campaigns during which the variability was probed over shorter timescales, the data are not well fit by a power law (probability for this fit is 4.9%).

(A color version of this figure is available in the online journal.)

well as in previous studies show roughly symmetric flares with comparable rise and fall times. By fitting the measured optical and X-ray structure functions to those generated from simulated light curves (composed of a random sequence of triangular flares) we derive a characteristic rise time of approximately 0.6 days in the X-ray variability, and between 10 and 20 days in the optical. This is in general agreement with the difference in cooling times for the electron populations generating the optical and X-ray synchrotron emission, where we expect

$$\tau_{\mathrm{cool,opt}} = \sqrt{\frac{\omega_X}{\omega_{\mathrm{opt}}}} \cdot \tau_{\mathrm{cool},X} \approx \sqrt{1000} \cdot 0.6\,\mathrm{days} = 19\,\mathrm{days}.$$

As detailed in the following paragraph, with the simple model adopted here, it is difficult to obtain a good fit to the rather hard power-law TeV emission without invoking extreme values for some of the model parameters (high Doppler factor, low magnetic field, and small emission region) perhaps indicating that a more detailed theoretical analysis is warranted. We find a low value for the magnetic field ($B \sim 0.12$ G) similar to the value of 0.1 G found by Lichti et al. (2008) during 2006 June. Their best fits, however, gave a significantly lower value for the Doppler factor ($\delta = 15$), compared with the value ($\delta = 90$) found here, which we note is similar to that found in some previous studies (Krawczynski et al. 2001; Rebillot et al. 2006). This high value for the Doppler factor results in some inconsistencies in the shock acceleration parameters namely, a very hard electron spectrum ($\sim E^{-1.5}$) contrary to the predictions for nonrelativistic diffusive shock acceleration (giving $E^{-2.0}$) or ultrarelativistic shock acceleration (giving $E^{-2.2}$). The acceleration efficiency would have to be quite low, with the mean free path for scattering ~20 times the Bohm limit and a shock velocity of $0.02c$, resulting in relatively few shock crossings. If the extreme parameters suggested by the simple model adopted here are correct, these observations lend some support to a new model for relativistic shock acceleration (Stecker et al. 2007), which predicts a spectral index of 1.5 or, they could indicate an even more dramatic departure from the shock-acceleration model, such as the Poynting jet model described in Krawczynski (2007). It is clear, however, that more detailed observations and modeling are necessary before stronger conclusions on such models can be drawn. The parameters used for both fits shown in Figures 20 and 21 are listed in Table 4. The only differences between the medium-state and high-state fits in these fits are the fraction of the optical light and the luminosity of the optical emitting region. We note that the flux in the X-ray band was higher and the spectrum harder on the "medium" state gamma-ray night and was lower and softer than this on the "high" state gamma-ray night.

For Mrk 501, Ghisellini et al. (2005) used external seed photons from a slow jet component to reproduce the TeV emission with lower Doppler factors. However, when we attempt to fit the Mrk 421 data in this way, we find that we can no longer fit the detailed shape of the declining X-ray and TeV spectrum. While there are too many free parameters to find a unique solution, or to draw definitive conclusions, it is clear that a large contribution from an EC component is a strong possibility for Mrk 421. While the data do not demand an EC component, the additional cooling may be present and can reduce the maximum energy for shock acceleration, somewhat mitigating the aforementioned problems. Increasing the cooling further quickly results in a Compton-catastrophe, overproducing the observed gamma-ray emission.

The radio portion of the SED is not well fit by this single-zone model. Although the TeV blazars are weak radio sources, the data have sufficiently good statistics to indicate that strong variability, characteristic of blazars at higher energies, is not present in the radio band so, it is likely that a different population of particles is responsible for the synchrotron emission at these energies.

The AGN monitoring campaign is ongoing at the Whipple 10 m Telescope. In addition to providing long-term light curves on TeV blazars, which are even more relevant now that the *Fermi Space Telescope* (formally *GLAST*) is providing long-term monitoring of the sky in the MeV–GeV energy range, these observations can also be used to trigger VERITAS and other VHE detectors when any of the AGNs bring monitored enter a high emission state (Swordy 2008).

The authors thank Emmet Roache, Joe Melnick, Kevin Harris, Edward Little, and all of the staff at the Whipple Observatory for their support. We also thank the anonymous referee for providing us with constructive suggestions, which were implemented to improve this paper. This research was supported in part by the US Department of Energy, the National Science Foundation, the Smithsonian Institution, Science Foundation Ireland, by PPARC in the UK, and by NSERC in Canada. The ASM quicklook results were provided by the ASM/*RXTE* teams at MIT and at the *RXTE* SOF and GOF at NASA's GSFC. The UMRAO team acknowledges the support of the NSF (AST 0607523) and the support of the University of Michigan. Y.Y.K. is a Research Fellow of the Alexander von Humboldt Foundation. RATAN-600 observations are partly supported by the Russian Foundation for Basic Research (projects 01-02-16812, 05-02-17377, 08-02-00545). The National Radio Astronomy Observatory is a facility of the National Science Foundation operated under cooperative agreement by Associated Universities, Inc. This research has made use of the MOJAVE (Lister & Homan 2005) and 2 cm survey (Kellermann et al. 2004) programs database. The Metsähovi team acknowledges support from the Academy of Finland. Acquisition and analysis of *Swift* data was supported at PSU through NASA grant NNX08AC38G, as part of the *Swift* Cycle 3 GI program.

REFERENCES

Aharonian, F. A. 2000, New Astron., 5, 377
Anton, M. 2007, http://www.mathworks.com/matlabcentral/fileexchange/loadFile.do?objectId=17466&objectType=FILE
Barthelmy, S. D. 2000, in Proc. SPIE 4140, X-Ray and Gamma-Ray Instrumentation for Astronomy XI, ed. K. A. Flanagan & O. H. Siegmund (Bellingham, WA: SPIE), 50
Beall, J. H., & Bednarek, W. 1999, ApJ, 510, 188
Błażejowski, M., et al. 2005, ApJ, 630, 130
Böttcher, M. 2007, Ap&SS, 309, 95
Bradt, H. V., Rothschild, R. E., & Swank, J. H. 1993, A&AS, 97, 355
Buckley, J. H. 2000, in AIP Conf. Proc. 516, 26th International Cosmic Ray Conference, ed. B. L. Dingus, D. B. Kieda, & M. H. Salamon (New York: AIP), 195
Burrows, D. N., et al. 2005, Science, 309, 1833
Catanese, M., et al. 1998, ApJ, 501, 616
Dar, A., & Laor, A. 1997, ApJ, 621, 181
Edelson, R. A., & Krolik, J. H. 1988, ApJ, 333, 646
Fossati, G., et al. 2000, ApJ, 541, 153
Fossati, G., et al. 2008, ApJ, 677, 906
Gehrels, N., et al. 2004, ApJ, 611, 1005
Ghisellini, G., Tavecchio, F., & Chiaberge, M. 2005, A&A, 432, 401
Giebels, B., Dubus, G., & Khélifi, B. 2007, A&A, 462, 29
Hillas, A. M. 1985, in Proc. 19th International Cosmic Ray Conference (La Jolla), ed. F. C. Jones, J. Adams, & G. M. Mason (Washington, DC: NASA–Scientific and Technical Information Branch), 3, 445
Horan, D., et al. 2002, ApJ, 571, 753
Hovatta, T., et al. 2007, A&A, 469, 899
Hu, S. M., Zhao, G., Guo, H. Y., Zhang, X., & Zheng, Y. G. 2006, MNRAS, 371, 1243
Inoue, S., & Takahara, F. 1996, ApJ, 463, 555
Jordan, M. M. 2004, PhD thesis, Washington Univ.
Kellermann, K. I., et al. 2004, ApJ, 609, 539
Kildea, J., et al. 2007, Astropart. Phys., 28, 182
Korolkov, D. V., & Parijskij, Y. N. 1979, Sky Telesc., 57, 324
Kovalev, Y. Y., et al. 1999, A&AS, 139, 545
Kovalev, Y. Y., et al. 2002, PASA, 19, 83
Kovalev, Y. Y., et al. 2005, AJ, 130, 2473
Krawczynski, H. 2007, ApJ, 659, 1063
Krawczynski, H., et al. 2000, A&A, 353, 97
Krawczynski, H., et al. 2001, ApJ, 559, 187
Krawczynski, H., et al. 2004, ApJ, 601, 151

Krennrich, F., et al. 2002, ApJ, 575, L9
Krimm, H. A. 2006, BAAS, 38, 374
Krimm, H. A. 2008a, http://swift.gsfc.nasa.gov/docs/swift/results/transients/
Krimm, H. A. 2008b, http://swift.gsfc.nasa.gov/docs/swift/results/transients/Transient_synopsis.html
Lebohec, S., & Holder, J. 2003, Astropart. Phys., 19, 221
Levine, A. M., et al. 1996, ApJ, 469, L33
Li, H., & Kusunose, M. 2000, ApJ, 536, 729
Lichti, G. G., et al. 2008, A&A, 486, 721
Lister, M. L., & Homan, D. C. 2005, AJ, 130, 1389
Mannheim, K. 1993, A&A, 269, 67
Mücke, A., et al. 2003, Astropart. Phys., 18, 593
Nilsson, K., Pursimo, T., Takalo, L. O., Sillanpää, A., Pietilä, H., & Heidt, J. 1999, PASP, 111, 1223
Pohl, M., & Schlickeiser, R. 2000, A&A, 354, 395
Punch, M., et al. 1992, Nature, 358, 477
Rebillot, P. F., et al. 2004, BAAS, 36, 912
Rebillot, P. F., et al. 2006, ApJ, 641, 740
Reynolds, P. T., et al. 1993, ApJ, 404, 206
Sambruna, R. M. 2007, Ap&SS, 311, 241
Spada, M., Ghisellini, G., Lazzati, D., & Celotti, A. 2001, MNRAS, 325, 1559
Stecker, F. W., Baring, M. G., & Summerlin, E. J. 2007, ApJ, 667, L29
Steele, D., et al. 2008, in Proc. 30th International Cosmic Ray Conference, ed. R. Caballero et al. (Mexico City: Universidad Nacional Autónoma de México), 989
Swordy, S. 2008, ATel, 1506, 1
Takahashi, T., et al. 2000, ApJ, 542, L105
Teräsranta, H., et al. 1998, A&AS, 132, 305
Vagnetti, F., & Trevese, D. 2003, Mem. Soc. Astron. Ital., 74, 963
Vagnetti, F., Trevese, D., & Nesci, R. 2003, ApJ, 590, 123
Vaughan, S., Edelson, R., Warwick, R. S., & Uttley, P. 2003, MNRAS, 345, 1271
Villata, M., Raiteri, C. M., Lanteri, L., Sobrito, G., & Cavallone, M. 1998, A&AS, 130, 305
Weekes, T. C., et al. 2001, Astropart. Phys., 17, 221
Yadov, K. K., et al. 2007, Astropart. Phys., 27, 447
Zhang, Y. H., Treves, A., Celotti, A., Qin, Y. P., & Bai, J. M. 2005, ApJ, 629, 686